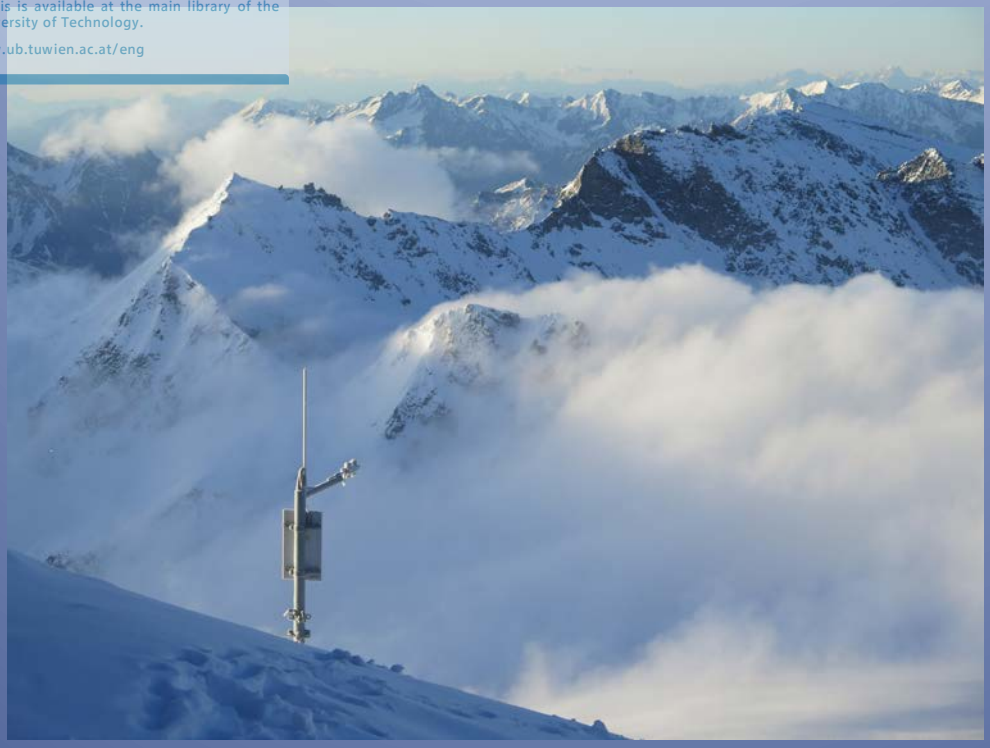

Electrical modelling for an improved understanding of GPR signatures in alpine permafrost

Theresa Maierhofer

TECHNISCHE UNIVERSITÄT WIEN
Vienna University of Technology

RESEARCH GROUP GEOPHYSICS

Master Thesis

Electrical modelling for an improved understanding of GPR signatures in alpine permafrost

ausgeführt zum Zwecke der Erlangung des akademischen Grades eines

Diplom-Ingenieurs

unter der Leitung von

Ass.-Prof. Dr.rer.nat. Adrian Flores-Orozco
(E120 Department für Geodäsie und Geoinformation, Forschungsgruppe: Geophysik)

Dipl.Ing. Matthias Steiner

(E120 Department für Geodäsie und Geoinformation, Forschungsgruppe: Geophysik)

eingereicht an der Technischen Universität Wien

Fakultät für Mathematik und Geoinformation

von

Theresa Maierhofer

1008537 (E 0664 421)

Wien, im März 2018

_____

Theresa Maierhofer

TECHNISCHE UNIVERSITÄT WIEN
Vienna University of Technology

Ich habe zur Kenntnis genommen, dass ich zur Drucklegung meiner Arbeit unter der Bezeichnung

Diplomarbeit

nur mit Bewilligung der Prüfungskommission berechtigt bin.

Ich erkläre weiters Eides statt, dass ich meine Diplomarbeit nach den anerkannten Grundsätzen für wissenschaftliche Abhandlungen selbstständig ausgeführt habe und alle verwendeten Hilfsmittel, insbesondere die zugrunde gelegte Literatur, genannt habe.

Weiters erkläre ich, dass ich dieses Diplomarbeitsthema bisher weder im In- noch Ausland (einer Beurteilerin/einem Beurteiler zur Begutachtung) in irgendeiner Form als Prüfungsarbeit vorgelegt habe und dass diese Arbeit mit der vom Begutachter beurteilten Arbeit übereinstimmt.

Wien, im März 2018

_____

Theresa Maierhofer

Danksagung

DANKE …

… an meinen Betreuer Adrian Flores-Orozco, für die Geduld und die Fähigkeit Menschen für ein Thema zu begeistern. Egal ob früh oder spät, beim fünften oder zehnten Café, ich konnte immer an seine Tür klopfen. Ich habe durch diese Arbeit nicht nur Wissen in der Geophysik erlangt, sondern eine Forschungsgruppe kennengelernt, die mir sehr ans Herz gewachsen ist.

… an Matthias Steiner, für die gemeinsam verbrachte Zeit, ob bei physikalischen oder politischen Diskussionen, einem Schnaps oder zwei. Ich werde die Sonnblickfahrten, so mühsam sie auch immer wieder aufs Neue waren, nie vergessen. Zusätzlich möchte ich mich auch für die Hilfe bei meiner Diplomarbeit bedanken.

… an Walter Loderer, für die mentale und liebevolle Unterstützung. Oft hilft bei einem Schreibtief eine Schachtel Schokobananen mehr als jedes wissenschaftliche Gespräch.

… an Werner Chwatal, für das offene Ohr gegenüber jeder noch so dummen Frage in der Geophysik. Ich habe bei den Gesprächen sehr viel gelernt und weit hinaus über den Tellerrand der Geophysik geblickt.

… an Martin Mayr, für die Hilfe bei den Messungen. Ohne ihn wäre ich wahrscheinlich heute noch nicht mit den Sonnblick Messungen fertig. Auch Jakob Gallistl möchte ich danken für seine Unterstützung.

… an meine Freunde, fürs Zuhören, Dasein und Wein trinken.

… an Georg, für deine Geduld, dein Verständnis und deine Fähigkeit mich abzulenken. Ohne dich hätte ich das nicht geschafft.

… an Mama, Papa und Stefanie, dafür dass es euch gibt und ihr in jeder Situation für mich da wart. Danke dafür, dass ihr mir das Studium ermöglicht habt und mich auf meinem Weg begleitet und bestärkt habt.

Kurzfassung

Im Rahmen der vorliegenden Diplomarbeit wurde im Gipfelbereich des Hohen Sonnblicks eine Serie von Georadar Messungen durchgeführt. Das Ziel dieser Messungen lag darin, die internen Strukturen und die Verteilung des alpinen Permafrosts und damit assoziierte Veränderungen aufgrund von Temperaturschwankungen zu bestimmen. Nachdem Georadar bereits erfolgreich zur Quantifizierung von gefrorenem Material in Permafrost Regionen eingesetzt wurde, organisierte die Forschungsgruppe Geophysik der TU Wien mehrere 3D-Kampagnen im Zeitraum von 2015 bis 2017. Verglichen mit bisherigen Studien lag das Augenmerk nicht nur in der Identifizierung von möglichen Schichtgrenzen, sondern in der Modellierung der elektrischen Eigenschaften des Untergrundes, um das allgemeine Verständnis und die Interpretation von Georadar und Geoelektrik Ergebnissen zu verbessern. Neben der Prozessierung und Interpretation der Rohdaten, wurde ein quasi-kontinuierliches Modell der elektrischen Eigenschaften des Untergrundes im Gipfelbereich des Hohen Sonnblicks bestimmt. Damit wurde eine Quantifizierung lithologischer Kontakte und Diskontinuitäten zur Bestimmung von Atmosphäre - Untergrund Interaktionen möglich. Der Modellierungsansatz wurde in drei Fallstudien in porösen und unbefestigten Materialien behandelt, um ihn in Schutt - Materialien am Sonnblick anzuwenden. Zur Validierung der Modellierungsergebnisse wurde ein Vergleich zwischen Bohrlochtemperaturdaten und Georadar Ergebnissen aufgestellt, welcher sich als konsistent erwies.

Abstract

In frame of this diploma thesis a series of Ground Penetrating Radar (GPR) surveys at the summit of Hoher Sonnblick were conducted. The objective was to determine the internal structures and distribution of mountain permafrost and associated changes due to seasonal variations in temperature. 3D GPR surveys organised by the Geophysics Research group of the TU Vienna, were repeated between 2015 and 2017 at different times, as GPR has successfully been applied to delineate frozen materials in permafrost regions. Nevertheless, in comparison with previous studies, GPR investigations aimed not only at the identification of possible interfaces, but to develop a methodology for the modelling of electrical properties of the subsurface that permits an improved understanding and interpretation of GPR and Electrical Resistivity Tomography (ERT) imaging results. Besides the processing and interpretation of the raw data, a quasi-continues model of the electrical properties in the subsurface at the summit of Hoher Sonnblick was obtained, regarding lithological contacts and discontinuities (e.g., fractures) controlling atmospheric-subsurface interactions. The modelling approach was tested on three case studies in porous and unconsolidated media and finally it was applied in the highly fractured media present at the Hoher Sonnblick. For validation, the GPR modelling results were compared to borehole temperature data revealing consistency.

Inhaltsverzeichnis

1 Introduction

„Permafrost is hidden beneath the surface and less in the public consciousness than sea ice, glaciers, and ice sheets, but it directly affects human and biological systems that live with it. Permafrost can be hundreds of metres thick and tens to hundreds of millennia in age, with a geologic intransience but recent changes that remind us that it is not so permanent a feature of the landscape as it seems…" (Shawn J. Marshall, 2012)

As we can see from this citation, climate warming is getting an increasingly important issue in today's human environment; and so the impact of warming-induced permafrost degradation is a new research area that established in the past decades (Hauck and Kneisel 2008). Permafrost or permanently frozen ground, defined as soil or rock that remains beneath 0°C for two or more years, is predominantly known from polar regions, as described by the (Subcommittee 1988). Those regions are characterised by plain and uniform surfaces with relatively homogeneous permafrost distribution facilitating the determination of location and extent of permafrost in the subsurface. A substantial part of the permafrost is considered as mountain permafrost, which in contrast is highly variable and strongly dependent on altitude, incoming radiation, local climate and geology. The subsurface is heterogeneous and consists mainly of loose debris and a very complex subsurface matrix, further described in (Hauck 2001).

Consequently, these heterogeneous permafrost conditions require methods that are able to resolve near subsurface conditions at scales between one to tens of metres. Point information from borehole data is not representative for a larger area to characterise the spatial distribution of permafrost (Kneisel et al. 2008). Since geophysical properties alter significantly for a change of aggregate state of water (water/ice), geophysical methods can be used to locate and characterise those changes (Harris et al. 2009).

In the early years of permafrost exploration, geophysical methods have been mainly applied in polar permafrost regions as for example in Barrow, Alaska (Hinkel et al. 2001). Today, geophysical methods like Electrical Resistivity Tomography (ERT) and Seismic Refraction Surveys are well established in mountain permafrost, which can be seen from various studies (Krautblatter et al. 2010; Kneisel et al. 2008; Mühll et al. 2001; Rogger et al. 2017). However, ERT measurements might be limited in winter due to the low current injections taking place in surfaces covered by snow and ice; thus, commonly resulting in measurements with a poor signal-to-noise ratio (SNR), as described by (Harris et al. 2009). The presence of snow and ice on the surface may also affect seismic methods, which also require a firm contact between the ground and the geophones to enhance SNR.

To overcome such limitation, previous studies in permafrost (Hauck and Kneisel 2008; Moorman, Robinson, and Burgess 2007) have successfully applied Ground Penetrating Radar (GPR), a contactless method based on the propagation of electromagnetic waves. GPR is a promising tool to delineate frozen materials in polar permafrost regions, where the depth of thaw within the active layer could be mapped very precisely (Hinkel et al. 2001). In addition, GPR was applied to map the internal structure of rock glaciers (Berthling et al. 2008; Rogger et al. 2017). However, the majority of previous studies in permafrost have mainly aimed at a qualitative interpretation of the features resolved by means of GPR data, without the derivation of subsurface electrical properties; thus impeding a quantitative estimation of thermal properties, as required to assess the impact of atmospheric effects in permafrost.

To better understand subsurface processes in permafrost environments, geophysical imaging results for data collected at the summit of Hoher Sonnblick are presented in this thesis. Located in the Hohe Tauern region (Austrian Central Alps) 3106 m above sea level (asl), different sensors are installed to gain information about different meteorological parameters. The Sonnblick Observatory is an outstanding research station concerning studies about atmosphere, hydrosphere, cryosphere, lithosphere and biosphere. Permafrost studies of the summit of Hoher Sonnblick can be found in (Schöner et al. 2012). Furthermore, a permanently installed monitoring array (Figure 1) permits the collection of ERT on a daily basis, which provides information about changes in the electrical resistivity in an imaging framework (Supper et al. 2014). Investigations performed by the TU-Wien between 2015 and 2017 included ERT monitoring campaigns, 3D Refraction Seismic Tomography (RST) and 3D monitoring campaigns with GPR.

The final objective of this thesis is to obtain a 3D subsurface model of the electrical properties at the summit of Hoher Sonnblick with high resolution for an improved characterization of the active layer and lithological contacts and discontinuities (e.g., fractures) controlling atmosphere-subsurface interactions. GPR measurements were collected at the study area using different antennas and settings. To improve the quantitative interpretation, the synthetic response was numerically modelled taking into account the resistivity distribution in the subsurface as derived from ERT results. To increase the reliability of the models, further information was added using borehole information. Moreover, GPR campaigns were performed at different times of the year to gain information about spatial and temporal changes in the GPR signatures, as needed for an improved understanding of seasonal variations in the active layer. For validation, the modelling approach is tested on three case studies in porous and unconsolidated media and finally it is applied in the highly fractured media present at the Hoher Sonnblick.

2 Permafrost at Sonnblick Observatory

This chapter provides a short overview on recent permafrost research at Sonnblick Observatory. As an introduction, the term permafrost, its occurrence and processes are explained focusing on mountain permafrost. The study area is described briefly to get an insight in the geology and climate at Sonnblick observatory.

2.1 Permafrost – Basic Considerations

The following description of permafrost is based on the Permafrost Review of (Dobinski 2011). Permafrost does not necessarily need to contain water or ice but is only defined via temperature. It is not a material phenomenon, but a physical state of the lithosphere that cannot be characterised by an explicit type of material, which makes its detection more difficult. If the permafrost consists of ice, it is assigned to the cryosphere where water is in solid state (glaciers, permafrost, snow, sea ice…). Permafrost occurs in regions where mean annual air temperature stands below -1° C, which is the case in subpolar and mountainous environments as for example on the summit of Hoher Sonnblick.

The occurrence of permafrost is linked to the fact that the extent of winter freezing of the ground exceeds the extent of summer thawing. In this case, a very thin layer of frozen ground develops due to climatic cooling. This layer remains till next winter with a permafrost table and a permafrost base, which is shown in Figure 2-1. If the cooling continues, the thickness of this layer increases year after year. Due to seasonal change, cold and heat penetrate the ground in turn. In winter, when temperatures fall far below 0° C, the ground is frozen from the surface to the depth of the maximum winter freezing. In summer, a part of the frozen ground at the surface as well as at the base is thawing. The surface layer is called an active layer (h_a) which thaws and refreezes at different depths depending on the temperatures in summer. The thickness of the active layer depends on several factors: ambient air temperature changing with altitude and geographic latitude; vegetation, incident solar radiation depending on exposition and slope, thickness of snow cover, heat capacity and heat permeability of the medium, etc. A driving factor in permafrost environments is the snow cover, as it covers the ground from heat or cold. If snow is falling already in early fall, the snow cover acts as an isolator from the cold outside and the ground stores the heat. If there is no snow fall till winter, the ground is able to cool down. The longer the snow cover stays in spring, the more the ground is protected and isolated from heat

supply. Also the ground material plays an important role, as blocky surface material filled with air isolates the ground from heat in summer and makes a cold air circulation possible in winter.

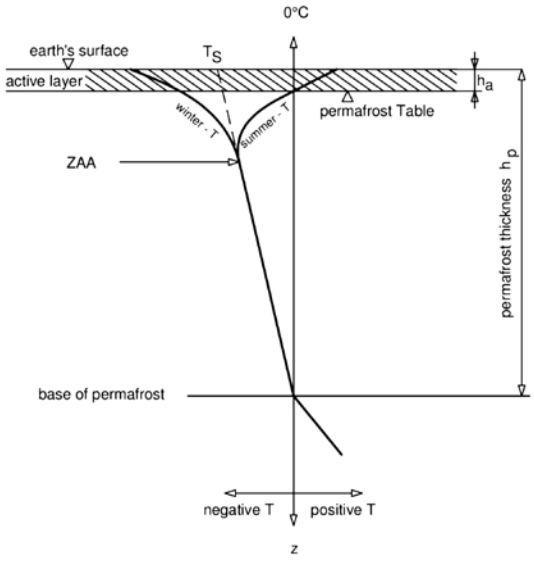

Figure 2-1: temperature profile of a permafrost ground

There are two basic forms of permafrost that can be distinguished: Arctic (polar), latitudinal permafrost which is mostly a few hundred metres thick and continuously distributed, and mountainous, altitudinal permafrost which is strongly variable.
Mountainous permafrost is dependent on altitude, slope exposition and topographic conditions. Therefore we differentiate between three types of mountainous permafrost (Krainer 2007):

- Active rock glaciers, consisting of debris and ice moving downslope. In Austria there are several hundreds of active rock glaciers where some of them have been successfully characterised by geophysical methods and can be found in (Hausmann et al. 2012; Rogger et al. 2017)
- Permafrost in loose debris which is commonly found 2200m asl and characterised by special surface features.
- Permafrost in bedrock which results from freezing water in fractures and crevices. This type of permafrost can be found in higher altitudes above 3000m asl. One example for permafrost in bedrock is the Hoher Sonnblick summit (Schöner et al. 2012; Krainer 2007)

2.2 Study Site Hoher Sonnblick

The study site Hoher Sonnblick is located 3106m a.s.l. in the Austrian Central Alps in the Goldberg Group on the border between Carinthia and Salzburg. As described by (Schöner et al. 2012), it is characterised by the complex geology of the "Tauernfenster" and the Alpine main

divide which is a clear climate border, visible in precipitation patterns and snow cover distribution. The summit is surrounded by the glaciers Kleinfleißkees and Goldbergkees.

2.3 Recent Permafrost Research at Sonnblick Observatory

The permafrost related research activities around the Sonnblick comprise amongst others an installation of three 20m deep boreholes equipped with temperature sensors, a permanently installed ERT profile which was established in the upper summit area, 15 geophones which were installed in the boreholes for passive seismic measurements and for the monitoring of rock fall activity and additional Bottom Temperature of Snow cover (BTS) measurements, as described by reports of different projects such as Person, SeisRock and Atmoperm. (Schöner et al. 2012) monitored the spatio-temporal patterns of permafrost with geophysical methods (GPR and seismic) and stated a debris cover of 2.5m with an active layer of 1.5m and a layer of jointed bedrock with open, probably ice-filled joints down to a depth of about 9m. Ongoing permafrost research within the Geophysics Research group at the Technical University of Vienna focuses on the quantification of the active layer at Sonnblick Summit by means of geophysical methods such as Refraction Seismic Tomography, Electrical Resistivity Tomography, Spectral Induced Polarisation methods, Electromagnetic Imaging, Transient Electromagnetic Sounding and Ground Penetrating Radar surveys.

2.4 Temperature data and geoelectrical measurements

Temperature data are measured within the three boreholes, which are located on the south-facing slope of the summit of Sonnblick with a separation between the boreholes of ~30m. The uppermost borehole is located next to the Sonnblick Observatory, whereas the lowest borehole is situated close to a permanent snow field and the nearby glacier Goldbergkees. The temperature data are provided from the University of Graz and discussed in the frame of the Atmoperm project. Temperature data are employed to validate GPR modelling results.

The infrastructure of the ERT monitoring profile installed by the GBA was occupied by the TU Vienna to perform ERT and Spectral Induced Polarisation (SIP) measurements. Within this thesis, the focus will be on ERT data used for the modelling of GPR data.

3 Geophysical Methods

In the following chapter a succinct overview of the concepts and physical issues of geophysical methods is provided which are utilised to gain information about the physical properties and the structure of the subsurface. In permafrost the key properties are temperature and ice content. These properties can only be observed directly by drilling a hole or with the help of geophysical methods such as GPR and ERT.

3.1 Ground Penetrating Radar

Ground penetrating radar is a near-surface geophysical method, first published by Leimbach and Löwy in 1910. It deploys a transmitter and a receiver moved over the surface to detect changes in subsurface electromagnetic impedance via the propagation and reflection of an electromagnetic wave at impedance boundaries (Everett 2013), as shown in Figure 3-1. The travel time of the wave is used to determine the wave velocity of the subsurface material. The frequency of GPR radio waves ranges from 10 MHz to 2 GHz, higher than in ERT methods. The transmitter generates a pulse of radiowaves at a defined frequency and the receiver is set to scan at a fixed rate in (scans per second). Each scan lasts as long as the two-way travel time range, which can be defined from a few tens to several thousand nanoseconds. The final product is a radargram, displaying the signals as a function of their amplitude and two-way travel time (Reynolds 2011). Unless otherwise stated, this chapter follows the description of (Butler 2005).

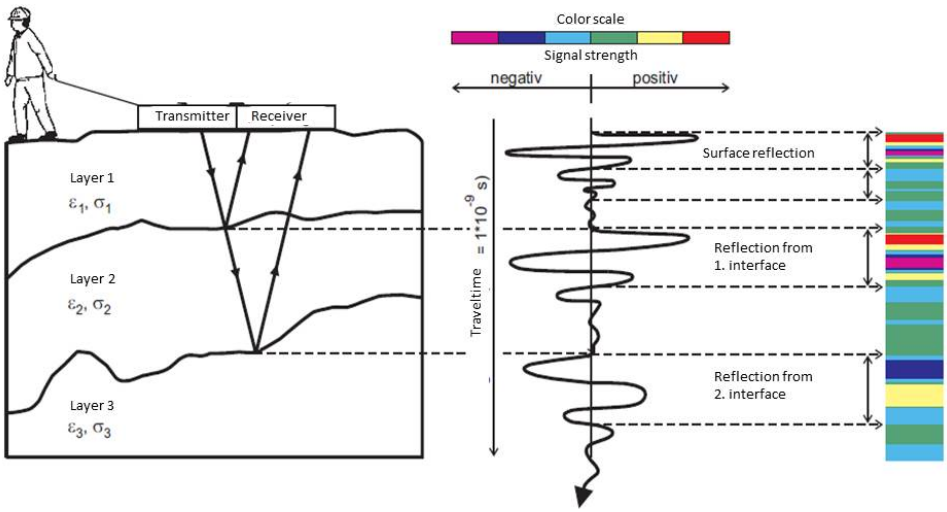

Figure 3-1: General principle of GPR showing one radar trace of a radargram with amplitude information and appropriate colour scale (Altekös ter 2004)

3.1.1 Propagation of electromagnetic waves

GPR has its foundations in electromagnetic theory and can thus be mathematically described by Maxwell's equations which explain the physics of electromagnetic fields. Constitutive relationships (Equation (3-1)-(3-3)) relate material physical properties to the electromagnetic fields. Hence, a material can be characterised by the response of the material (electrons/atoms/molecules/ions) to the application of an electromagnetic field. For GPR the electric and magnetic properties are important:

- Dielectric permittivity ε,

$$\boldsymbol{D} = \varepsilon \cdot \boldsymbol{E} = \varepsilon_0 \varepsilon_r \cdot \boldsymbol{E} \,, \tag{3-1}$$

  describes how constrained charges are displaced in response to an electric field, where D is the electric displacement vector [C/m^2], E is the electric field strength vector [V/m], ε_r is the relative electrical permittivity and ε_0 is the permittivity of vacuum (8.85 x 10^{-12} in [F/m]).

- Electrical conductivity σ,

$$\boldsymbol{J} = \sigma \cdot \boldsymbol{E} \,, \tag{3-2}$$

  describes how free charges move to create an electric current when applying an electric field, where J is the electric current density vector [A/m^2] and σ is the electrical conductivity [S/m].

- Magnetic permeability μ,

$$\boldsymbol{B} = \mu \cdot \boldsymbol{H} = \mu_0 \mu_r \cdot \boldsymbol{H} \,, \tag{3-3}$$

  describes the ability of a material to get magnetized when imposing an EM field on the material, where B is the magnetic flux density vector [T], H is the magnetic field strength vector [A/m], μ_r is the relative magnetic permeability and μ_0 is the free space permeability (4π x 10^{-7} in [H/m]).

Natural media can be dispersive, so ε, μ and σ are dependent on frequency and have to be treated as complex quantities. However, for most GPR applications, the scalar constant form of ε, σ, and μ is sufficient. Electrical properties are further described in section 3.1.2.

In order to explore the wave character of EM fields, simple media are discussed where material properties are assumed isotropic, independent of frequency and linear. As a charge moves, it implies a current J which generates a magnetic field B inducing an electric field E, which causes

the electric charge to move. This continuation of one field inducing the other results in fields propagating through the medium, as depicted in Figure 3-2.

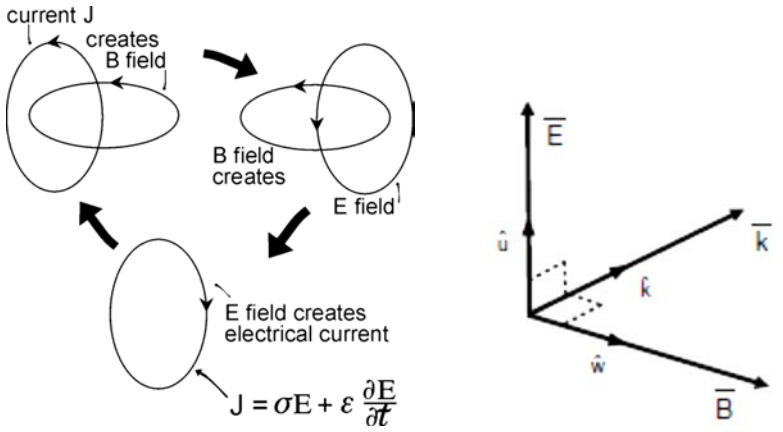

Figure 3-2: (left) Changing electric fields create magnetic fields which in turn induce electric fields which can be expressed by the transverse vector wave equation; (right) plane wave solution with electric, magnetic and propagation direction forming a 3D vector space.

Mathematically, the propagation of an EM wave is described by the transverse vector wave equation which is formed by the combination of Faraday's law, Ampere's law and the constitutive relations:

$$\nabla \times \nabla \times \boldsymbol{E} + \mu\sigma \frac{\delta \boldsymbol{E}}{\delta \boldsymbol{t}} + \mu\varepsilon \frac{\delta \boldsymbol{E}}{\delta \boldsymbol{t}^2} = 0 \qquad (3\text{-}4)$$

The closed circulation character of the magnetic field can be expressed in terms of the electric field. Both, electric and magnetic field satisfy the transverse wave equation. Solving for one field allows an immediate solution for the other. Solutions to the equation take the form depicted in Figure 3-2 (plane wave solutions). The magnetic and electric fields are perpendicular to each other and move in a direction perpendicular to both fields, the direction of the propagation constant k. By transforming the vector wave equation into the frequency domain by a Fourier transformation assuming sinusoidal time variation, the propagation constant can be expressed as follows:

$$k = \sqrt{\omega^2 \varepsilon\mu + i\omega\mu\sigma} = \frac{\omega}{v} + i\alpha \ , \qquad (3\text{-}5)$$

where ω is the angular frequency, v is the phase velocity and α is the attenuation. Real earth materials generally exhibit losses attributable to electrical conductivity. If those losses are low, which means that

$$\omega\mu\sigma \ll \omega^2 \varepsilon\mu \ , \qquad (3\text{-}6)$$

or

$$\frac{\sigma}{\omega\varepsilon} \ll 1 \ , \tag{3-7}$$

the wave properties (v, α and EM impedance Z) reduce to

$$v = \frac{1}{\sqrt{\mu\varepsilon}} = \frac{1}{\sqrt{\mu_0\varepsilon_0}} \frac{1}{\sqrt{\mu_r\varepsilon_r}} = \frac{c_0}{\sqrt{\varepsilon_r}} \ , \tag{3-8}$$

$$\alpha = \frac{\mu\sigma v}{2} \ , \tag{3-9}$$

and

$$Z = \sqrt{\frac{\mu}{\varepsilon}} \tag{3-10}$$

where c_0 is the speed of light in vacuum (c_0=299 792.458 m/s). The electromagnetic impedance Z states that the relative amplitude of electric and magnetic fields in our solutions are determined by the material properties.

The variation of the wave properties v and α for a medium with varying electrical conductivity versus sinusoidal frequency are shown in Figure 3-3 and further described by (Everett 2013). At low frequencies, wave properties depend on frequency. As frequency increases toward the water relaxation frequency in the 10 GHz - 20 GHz range, water absorbs energy more strongly and also scattering losses become important at high frequencies. In the GPR frequency range 10 MHz - 2GHz, the velocity is independent of both frequency and conductivity, which can be seen in Figure 3-3a. In Figure 3-3b, the dependence of attenuation on frequency and different conductivities is shown. High conductivity and high frequency values result in large signal attenuations and thus shallow penetration depths. Therefore, GPR is ineffective in high conductive materials where energy storage is small compared to energy dissipation (see Equation 3-4). The depth of penetration of GPR decreases as the product σω increases. To determine radar range, also instrumental factors need to be taken into account. The total path loss is composed of antenna losses, transmission losses between the air and the ground, losses caused by geometrical spreading of the radar beam, attenuation within the ground as a function of the material properties and losses due to scattering of the radar signal from the target itself. To account for all those terms, the radar range equation defines the radar system performance. For a detailed description of this equation please refer to (Reynolds 2011).

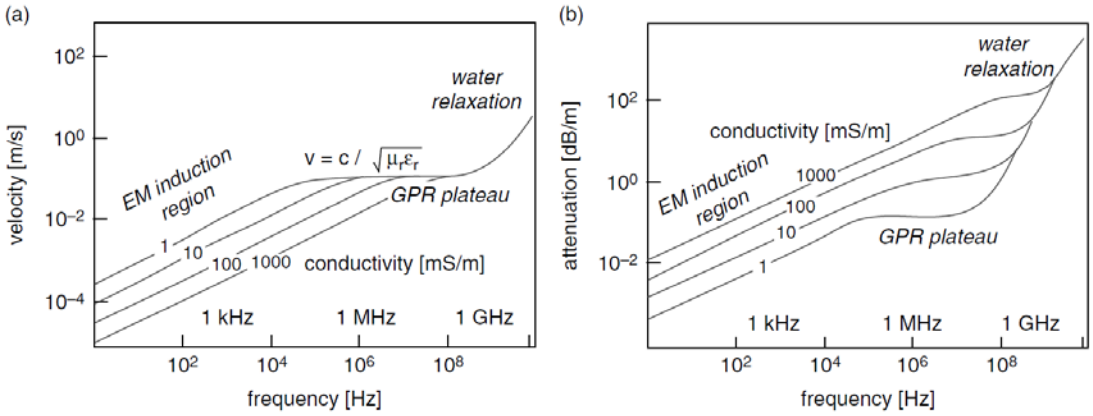

Figure 3-3: (a) GPR wave velocity as a function of frequency; (b) GPR attenuation as a function of frequency in (Everett 2013)

3.1.2 Electrical Permittivity and Conductivity – electrical properties of the subsurface

In most geological applications the GPR response is mainly controlled by the electrical properties ε and σ. Magnetic variations are usually very small and μ can be assumed to be equivalent to μ_0, the free space permeability (Butler 2005).

An electric field in a material causes electric charges to move (i.e., electric current). We differentiate between two types of charge in a material, namely, bound and free charges. These give rise to two types of current flow in any natural material, which are called conduction j_C and displacement j_D currents. Thus, the total current j in a medium is given through

$$\boldsymbol{j} = \boldsymbol{j_C} + \boldsymbol{j_D} \tag{3-11}$$

and

$$\boldsymbol{j} = \sigma \boldsymbol{E} + \varepsilon \frac{\boldsymbol{dE}}{\boldsymbol{dt}} \ . \tag{3-12}$$

The transition frequency defines the frequency above which displacement currents exceed conduction currents and is defined through the electrical conductivity and permittivity

$$\omega_t = \frac{\sigma}{\varepsilon} \ . \tag{3-13}$$

Since the two material properties affect radar wave propagation in different ways, it is necessary to examine the relationship between them more closely.

Permittivity

Permittivity describes the ability of a material to polarize and to store and release EM energy in the form of electric charge in response to an external electric field (Cassidy 2009). When a material is subjected to an external electric field, the atoms undergo different kinds of polarisation phenomena relevant to GPR, as depicted in Figure 3-4:

- (atomic polarization)
- molecular polarization
- interfacial polarization.

The atomic approach is a good way to illustrate how EM energy interacts with a material. Considering a material, consisting of atoms with positively charged nucleus and negatively charged electron atmospheres; the charges are unpolarised and there is a net zero charge across the material. An applied electric field **E** exerts a force on the electron atmosphere and displaces its charge centre, so the charges become "polarized" in relation to their original position. This phenomenon can be seen in Figure 3-4a and is called the "atomic polarization", as described in (Everett 2013).

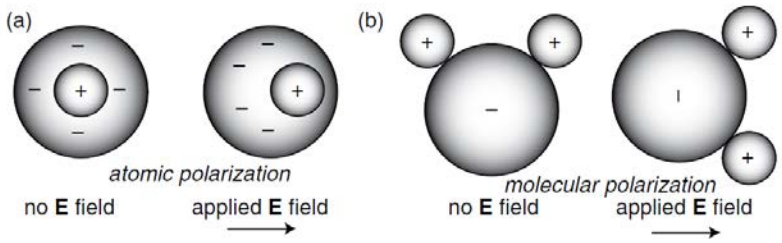

Figure 3-4: (a) Atomic Polarization; (b) molecular polarization (polarization of a water molecule) (Everett 2013)

If an electric field is applied on free charges (as in the case of polar water molecules), it will experience a torque so that the charges distribute into the direction of the applied field, which is demonstrated in Figure 3-4b. This rotation of the polar molecule causes energy dissipation introducing a component of dielectric loss into the polarisation process that acts out of phase with the energy storage mechanism. This polarization phenomenon is called "molecular or dipolar polarization", further described by (Everett 2013). (Cassidy 2009) states, that molecular polarization of bound and/or free charges (usually water molecules) largely controls the propagation of electromagnetic waves in the GPR frequency range, which is shown in Figure 3-5. Atomic polarization only plays a role at high frequencies (greater than 10 GHz) and in arid and glacial environments. Interfacial polarization or the Maxwell-Wagner effect becomes important at

frequencies less than 100 MHz. Interfacial-polarization occurs, as an electric field is imposed on a heterogeneous medium. The free charges are separated to form an induced dipole moment across the material causing the free charges to accumulate at dielectric interfaces. Thus, this polarization phenomenon is particularly important for low-frequency applications in fine-grained, saturated, porous media (Everett 2013; Cassidy 2009).

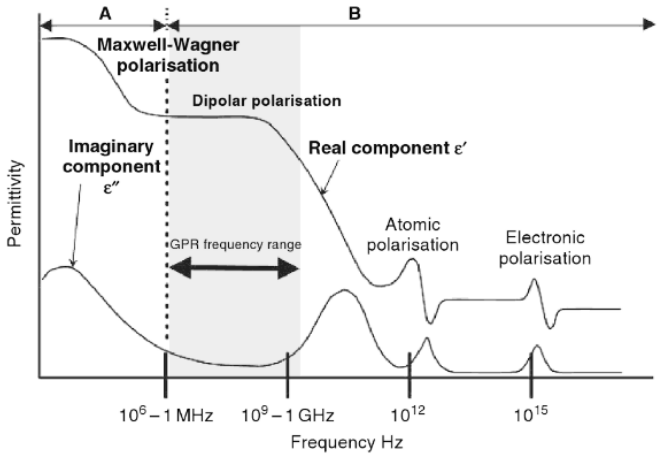

Figure 3-5: Polarisation phenomena associated with an idealised, lossy dielectric material (Cassidy 2009)

The electrical properties of natural materials are dispersive (frequency-dependent) at GPR frequencies (Everett 2013), which implies that permittivity is represented as a complex quantity that consists of a storage component (real permittivity ε') and a dissipation component (imaginary permittivity ε"). Thus, the complex permittivity is given by:

$$\varepsilon^* = \varepsilon' + i\varepsilon'' \quad . \tag{3-14}$$

The frequency dependence of the polarisation process is a manifestation of the permittivity relaxation phenomena where the time-dependent displacement mechanism is acting at different rates to the applied electric field, as reported by (Cassidy 2009). The temporal response of this process is described by a relaxation time τ and is related to the relaxation frequency by $f_{relax}=1/2\pi\tau$. If a material is subjected to an alternating electric field with a frequency below the relaxation frequency, the particles are able to react quickly enough to the applied field and stay in phase with its changes. Thus, energy is passed to the molecules as the field increases and is released with a decreasing field value. This procedure is called an energy storage and release mechanism, represented by the real permittivity. Whereas, as the frequency increases in the range of the relaxation frequency, the polarization of atoms and molecules is too slow to keep pace with the rapidly changing alternations of the applied field (Everett 2013). Consequently, less energy is passed to the molecules and the value of the real permittivity decreases. The molecules spend most of their time in motion, generating an out-of-phase displacement current and energy loss as heat. The value of the imaginary permittivity increases. At frequencies above the relaxation

frequency, the real and imaginary permittivity values drop as water molecules are not able to respond to such fast fluctuations in the electric field.

The real permittivity is a measure of a material's polarization and energy storage and can be described by

$$\varepsilon' = \varepsilon_r \cdot \varepsilon_0 \tag{3-15}$$

where ε_r is the relative permittivity, which varies from 1 in air to 81 in water. For most geological materials, ε_r lies in the range of 3-30. As water has an anomalously large relative permittivity due to the high polarizability of the water molecule in the presence of an applied electric field, water-bearing rocks have significantly higher relative permittivity values (ε_r~10-30) than dry rocks of the same lithology. Hydrocarbons such as oil and natural gas show low relative permittivity values (ε_r~1-2). A list of relative permittivity values and associated radar velocities for a variety of geological materials are given in Figure 3-7.

The imaginary permittivity is a measure of a material's loss of energy or absorption within the material. If the material is conductive, an additional term has to be included in the definition of the complex permittivity, as conductivity contributes to the loss within the material.

For an ideal dielectric as in the case of water and ice, Debye developed a relaxation model, which is applicable for a material with a single relaxation frequency and represented by the simple analytic form for the real permittivity (Artemov and Volkov 2014)

$$\varepsilon' = \varepsilon_\infty + \frac{\varepsilon_s - \varepsilon_\infty}{1 + \omega^2 \tau^2} \ , \tag{3-16}$$

and the imaginary permittivity

$$\varepsilon'' = (\varepsilon_s - \varepsilon_\infty) + \frac{\omega\tau}{1 + \omega^2 \tau^2} \tag{3-17}$$

where τ is the relaxation time, ω the angular frequency, ε_s the static permittivity and ε_∞ the high frequency limit of the permittivity. The permittivity spectrum of water and ice at 0°C is illustrated in Figure 3-6, showing the real $\varepsilon'(\omega)$ and imaginary permittivity $\varepsilon''(\omega)$ and the dynamical conductivity $\sigma_D(\omega)$. The characteristic peak of $\varepsilon''(\omega)$ and step of $\varepsilon'(\omega)$ at a frequency f_{relax} can be observed for water and ice and is known as the Debye relaxation. It is similar for both, water and ice, but shifted in frequency by six decades. As stated by (Cassidy 2009), for higher air temperatures, the permittivity spectrum of water shifts up-frequency, which means that losses will start to have a significant affect for high frequency surveys. At 0° C, losses are relevant above 100 MHz. When water freezes, the molecules form ionic bonds and the relaxation takes place in

the kilohertz range. This is why GPR losses are insignificant small and radar waves are able to penetrate very deep in ice.

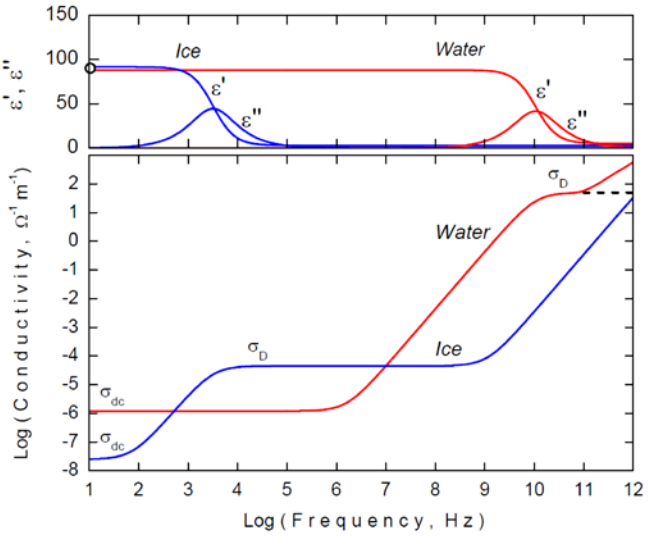

Figure 3-6: Permittivity and conductivity spectrum of water and ice at 0° C showing the real and imaginary permittivity and the dynamical conductivity (Artemov and Volkov 2014)

As natural materials do not mainly consist of water and ice, but are composed of liquids, solids and gases, the complex permittivity behaviour of the subsurface is best described by Cole and Cole. It includes an additional broadening factor α, which represents a distribution of individual relaxation times. The complex permittivity is described by (Cassidy 2009)

$$\varepsilon^* = \varepsilon_\infty + \frac{\varepsilon_s - \varepsilon_\infty}{1 + (\omega^2 \tau^2)^{1-\alpha}} \quad , \tag{3-18}$$

with α varying between 0 and 0.7.

Conductivity

The electrical conductivity is a measure of the charge transport within a material under the excitation of an external electric field and is described as a complex quantity

$$\sigma^* = \sigma' - i\sigma'' \tag{3-19}$$

where the real part represents the conduction current which is in phase with the driving voltage and the imaginary component describes the displacement current generated by lossless polarization effects and is out of phase. The complex permittivity, the complex conductivity and the complex resistivity are interrelated and describe the electrical behaviour of a medium.

$$\sigma^*(\omega) = \frac{1}{\rho^*(\omega)} = i\omega\varepsilon_0\varepsilon^*(\omega) \tag{3-20}$$

There are three mechanisms of conduction taking place in the near subsurface: electronic conduction, electrolytic conduction and surface conduction. Electrolytic conduction is the dominant process in near-surface rocks, taking place in connected pore spaces, along grain boundaries, in fractures, in faults and in shear zones (Ward 1988). It describes the movement of ions in response to an applied electric field. The ions which conduct the current result from dissociation of salts in groundwater. The solution with the higher density, charge and mobility of ions will have the higher conductivity (Butler 2005). Electrolytic conduction is dependent on porosity and the conductivity of the pore fluid, as shown by Archie's second law:

$$\sigma_0 = \frac{\Phi^m}{a}\sigma_f S^n + \sigma_c \tag{3-21}$$

where

- Φ… fractional pore volume (porosity)
- σ_f… pore fluid conductivity
- σ_0… bulk conductivity
- σ_c… soil grain surface conductivity
- m… cementation factor (1.4-2.2)
- a… coefficient of saturation (0.6-1.0)
- S… fractional water saturation, the fraction of the pores containing water
- n… saturation exponent (~2).

As temperature increases, the viscosity of water decreases and so the mobility of ions increases resulting in a higher conductivity value (Ward 1988).

In Figure 3-7 electrical conductivity values are given for different subsurface materials.

MATERIAL	ε	σ (mS/m)	v (m/ns)	a (dB/m)
Air	1	0	0.30	0
Distilled Water	80	0.01	0.033	2xl0-3
Fresh Water	80	0.5	0.033	0.1
Sea Water	80	3xl03	.01	103
Dry Sand	3-5	0.01	0.15	0.01
Saturated Sand	20-30	0.1-1.0	0.06	0.03-0.3
Limestone	4-8	0.5-2	0.12	0.4-1
Shales	5-15	1-100	0.09	1-100
Silts	5-30	1-100	0.07	1-100
Clays	5-40	2-1000	0.06	1-300
Granite	4-6	0.01-1	0.13	0.01-1
Permafrost	4-8	0.01 - 1	0.1 – 0.15	0.01
Ice	3-4	0.01	0.16	0.01

Figure 3-7: Typical electrical permittivity, electrical conductivity, velocity and attenuation observed in common geologic materials

3.1.3 Reflection & transmission at interfaces

GPR geophysical imaging is based on the reflectivity of the subsurface under investigation. If a radar pulse is incident on the boundary between two materials with different electrical properties, the direction of travel changes according to Snell's law and the varying amplitudes of the EM fields across the interface between the two materials can be quantified by the Fresnel reflection and transmission coefficients, as described by (Butler 2005).

For low loss materials, Snell's law takes the form

$$\frac{\sin\theta_1}{v_1} = \frac{\sin\theta_2}{v_2} \quad . \tag{3-22}$$

When a plane EM wave hits a boundary, it is partially reflected and transmitted. Thus, the reflection coefficient R and transmission coefficient T describe the ratio of the reflected/transmitted amplitude to the incident amplitude. When planar boundaries are encountered, EM waves separate into two independent components, which are referred to as the TE (transverse electric field) and TM (transverse magnetic field), shown in Figure 3-8.

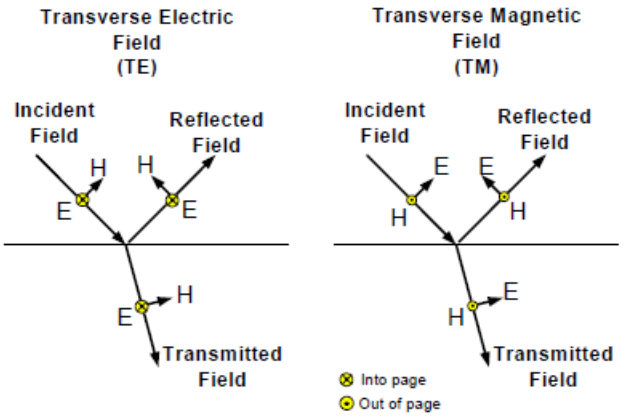

Figure 3-8: Reflected and transmitted transverse vector wave fields for planar interfaces (Butler 2005)

The reflection and transmission coefficients for TE and TM waves are expressed as

$$R_{TE} = \frac{Y_1 \cdot \cos\theta_1 - Y_2 \cdot \cos\theta_2}{Y_1 \cdot \cos\theta_1 + Y_2 \cdot \cos\theta_2} \tag{3-23}$$

$$R_{TM} = \frac{Z_1 \cdot \cos\theta_1 - Z_2 \cdot \cos\theta_2}{Z_1 \cdot \cos\theta_1 + Z_2 \cdot \cos\theta_2} \tag{3-24}$$

and

$$T_{TE} = 1 + T_{TE} \tag{3-25}$$

$$T_{TM} = 1 + R_{TM} \tag{3-26}$$

where Z_i and Y_i are the impedances and admittances ($Y_i=1/Z_i$) of the ith material. The reflection coefficient for a normally incident radar plane wave propagating in a non-magnetic ground, becomes

$$R = \frac{Z_2 - Z_1}{Z_2 + Z_1}\ , \tag{3-27}$$

as there is no difference between a TE and a TM wave, thus the reflection coefficients become identical. Therefore, R is an important descriptor of how much energy is reflected by radar waves at electrical boundaries.

The polarity of the reflection coefficients can be positive or negative depending on which impedance value is larger or smaller. The polarity of an incident GPR signal has the typical form of an M-shaped pulse (positive polarity) or a W-shaped pulse (negative polarity). The return signal from subsurface reflections can have the same shape or be inverted (opposite polarity) to the incident signal. The direct air-wave has the same shape as the incident signal (here M-shaped), whereas the ground wave will show a negative polarity, as depicted in Figure 3-9. The polarity of the reflection from subsurface horizons is dictated by the electrical properties that cause the reflection.

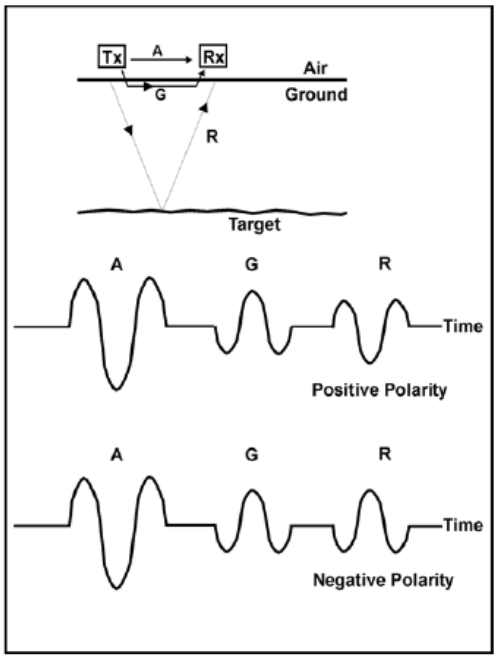

Figure 3-9: Polarity of GPR signals for direct air-wave, ground wave and reflected signal which could have either a positive or a negative polarity (Butler 2005)

3.2 Electrical Resistivity Tomography

The electrical resistivity tomography (ERT) is a well-established geophysical method for imaging subsurface structures to characterize groundwater, coal, faults, saltwater intrusion, contaminant plumes and a lot more environmental issues (Ward 1988). ERT has been successfully applied in permafrost environments (Harris et al. 2009) and investigations at the summit of Hoher Sonnblick benefit from the existence of an ERT monitoring profile (Supper et al. 2014). The resistivity (inverse of the conductivity) distribution of the subsurface is determined and used as an input parameter for the modelling of GPR data. Therefore, the basics of ERT are given in this section.

ERT is a method at low frequencies (typically 3 Hz to 0.03 Hz) where the current is injected into the ground between two electrodes and a voltage is measured between two other electrodes. If the electrodes are placed at the surface of a homogeneous half-space, then the current flows radially out through a hemisphere of radius r and surface area $2\pi r^2$. In a four electrode array (Figure 3-10:), the current enters the earth via one electrode C_1, exits via the other C_2 and the potential difference is measured between P_1 and P_2, so that we write

$$\Delta V = \frac{\rho I}{2\pi r}\left[\frac{1}{r_1} - \frac{1}{r_2} - \frac{1}{r_3} + \frac{1}{r_4}\right], \tag{3-28}$$

where I is the current, r_1 is the distance between P_1 and C_1, r_2 is the distance between P_1 and C_2, r_3 is the distance between P_2 and C_1, r_4 is the distance between P_2 and C_2, and ρ is the resistivity of a half-space which is then given by

$$\rho = \frac{\Delta V}{I} \cdot K\ , \tag{3-29}$$

with K representing the geometric factor. In the case of a homogeneous subsurface, ρ is called the *true resistivity*, whereas for an inhomogeneous earth, the resistivity varies with position and direction of the electrode array. Thus, the measured resistivity values are named *apparent resistivity*.

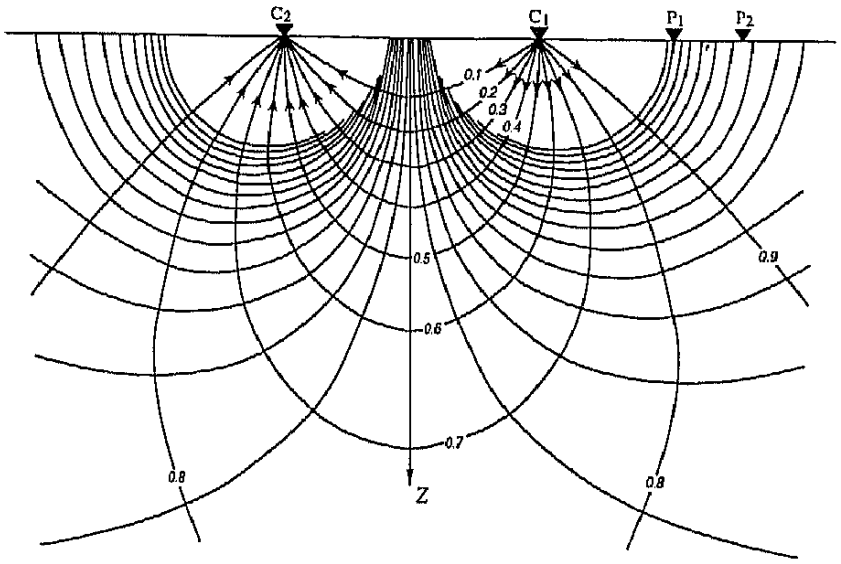

Figure 3-10: Current electrodes C_1 and C_2 and potential electrodes P_1 and P_2 are placed on the surface of a homogeneous half-space. The distribution of the current and potential lines is shown (Ward 1988).

The geometric factor of Equation 3-29 depends upon the measurement configuration (profile length, distance between electrodes,…) which is important for the exploration depth and resolution of the data, as described by (Knödel, Krummel, and Lange 2013). The most common arrays investigated in resistivity surveys are the dipole-dipole array, the gradient-array, the pole-dipole array, the schlumberger- and the wenner-array. Multi-electrode-arrays allow the collection of a great amount of data, which, in combination with inversion algorithms, enable the quantification of the quasi-continuous distribution of resistivity in the subsurface.

4 Acquisition and Processing of GPR Data

Alpine environments are not easy to access; therefore an optimized data acquisition requires planning. This chapter builds on the discussions of (Butler 2005) and gives a short overview on the resolution of GPR data, the planned survey design, different acquisition modes tested in permafrost environments, the processing of GPR data and an introduction to the velocity analysis.

4.1 Resolution and zone of influence

Resolution is a fundamental concept applicable to most wave phenomenon-based detection methods and an indicator how accurately a position can be determined and what kind of information can be extracted about the geometrical attributes of the illuminated target (shape, size, thickness, etc.). Resolution can be divided into two components, the longitudinal or range resolution length and the lateral or angular resolution length, depicted in Figure 4-1.

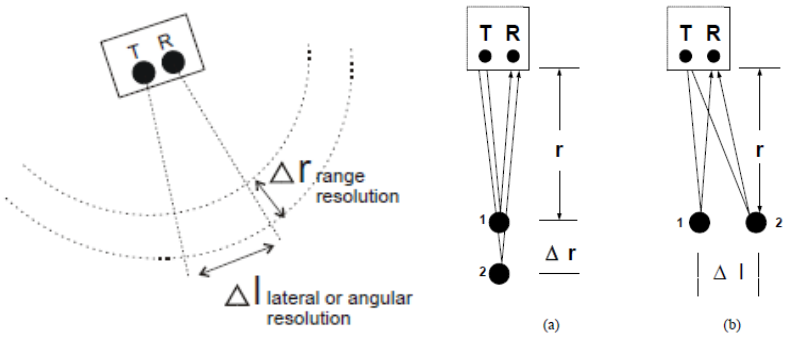

Figure 4-1: Range resolution and lateral resolution for the response of two localized targets, (a) in range or (b) side-by-side

In order to distinguish the response of two point targets 1 and 2 from Figure 4-1a, the two pulses have to be separated by half their half width and thus, the range resolution length can be expressed as

$$\Delta r \geq \frac{Wv}{4} = \frac{\lambda_c}{4} \quad . \tag{4-1}$$

From this equation we can see that the radial resolution is dependent on the pulse width W and the velocity (or the center wavelength λ_c) in the material and independent of distance from the source except for larger distances, where dispersion and attenuation will affect range resolution.

The lateral resolution (Figure 4-1b) depends on the velocity, the pulse width and the distance from the source and is closely related to the Fresnel zone concept for monochromatic signals through

$$\Delta l \geq \sqrt{\frac{vrW}{2}} = \sqrt{\frac{r\lambda_c}{2}} \ . \tag{4-2}$$

The larger the distance between the source and the target, the lower is the lateral resolution.

4.2 Survey Design

The survey design of common GPR measurements is presented in this section. It is a helping tool for the scheduling of GPR surveys. Basic considerations are made about the measurement mode, selection of operating frequency and time window, temporal and spatial sampling intervals.

4.2.1 Common Offset Mode

Common Offset or Constant Offset profiling with a continuously moving antenna is a standard acquisition mode, where the transmitter and receiver are separated by a fixed offset and moved along the survey line. The antennas are deployed in a fixed geometry (with a defined antenna separation and orientation) and as a measurement mode either a continuous mode with a definable sampling interval or a point mode can be selected. The intention of common offset reflection surveys is to map subsurface reflectivity versus spatial position. Variations in reflection amplitude and time delay imply variations in v, α and Z. The velocity of the medium can be detected by diffraction hyperbola analysis, further described in section 4.5. The parameters essential in common-offset surveys are the GPR center frequency, the recording time window, the temporal sampling interval, the spatial sampling interval, the separation between profiles in a grid and the antenna orientation. These parameters may be determined by the user depending on the specific GPR system, and are briefly summarised in this chapter.

4.2.2 Selecting operating frequency

The selection of the operating frequency is a trade-off between spatial resolution, clutter limitations, depth of penetration and system portability. In order to achieve a desired spatial resolution, a minimum center frequency is required

$$f_c^R > \frac{75}{\Delta x\sqrt{\varepsilon_r}}[MHz] \ , \tag{4-3}$$

where Δx is the spatial sampling interval. The radar response of heterogeneities and small-scale features in soils and rocks refers to clutter and increases as radar frequency increases. In order to limit the amount of energy scattered by clutter, (Butler 2005) states that the signal wavelength should be a factor ten longer than the clutter dimension ΔL and thus, the clutter center frequency takes the form

$$f_c^C > \frac{30}{\Delta L\sqrt{\varepsilon_r}}[MHz] \ . \tag{4-4}$$

4.2.3 Estimating the recording time window

The time window determines how long the system will record signals from the receiver antenna after a pulse has left the transmitter antenna. The necessary recording time window is dictated by the maximum depth and minimum velocity likely to be encountered in the study area. (Butler 2005) gives an estimate for the planning of GPR surveys

$$W = 1.3\frac{2 \cdot d_{\max}}{v_{\min}} \ . \tag{4-5}$$

4.2.4 Temporal sampling interval

The time interval between points on a recorded waveform, namely the temporal sampling interval, is controlled by the Nyquist sampling concept. The sampling frequency should be at least twice as high as the highest frequency of the record, in order to reproduce it correctly. The signals transmitted by a GPR antenna show frequencies within the interval $\langle 0.5f, 1.5\mathrm{f} \rangle$ where f is the center frequency of the antenna. The data should be sampled at a rate of 6 f_c

$$\Delta t = \frac{1}{6 f_c} \ . \tag{4-6}$$

4.2.5 Spatial sampling interval

The spatial sampling interval is the horizontal distance between discrete radar measurements and shouldn't be greater than the sampling interval from Equation (4-3)

$$\Delta x = \frac{c}{4 f_c \sqrt{\varepsilon_r}} = \frac{75}{f_c \sqrt{\varepsilon_r}} \ , \tag{4-7}$$

in order to properly image steeply dipping reflectors.

4.3 Important Processing Steps

The standard processing steps described below are performed on raw GPR data in order to transform measured travel times into a depth section that is ready for interpretation, further described by (Everett 2013) and (Butler 2005).

The first processing step is the *editing* and rearranging of the acquired GPR data. The data are converted to an editable format, files are merged, and traces are removed. As most processing algorithms require uniform spatial sampling intervals, missing traces can be restored by interpolating from neighbouring traces.

An essential processing step is the *time-zero correction*, where the radar traces of a profile are individually shifted along the time axis such that the first peak of the earliest arriving pulse is set to a common temporal datum.

In order to remove very-low-frequency components contained in the spectrum of the transmitted electric field, temporal filtering referred to as *dewowing* is applied to the data as a basic processing step. An alternative to the de-wow filter is the *bandpass filter*, which does not affect the signal shape and simultaneously gets rid of high frequency or monochromatic noise.

The waves are losing significant energy during travelling through the subsurface due to geometrical spreading and scattering attenuation. There are different time-dependent *gain functions* available in order to compensate the rapid fall off in radar signals from deeper depths.

One common processing step applied to GPR data is the *background-removal filter*, a form of spatial filtering, which involves the subtraction of a lateral moving average of the signal amplitudes from each radar trace over a given time window. This filter is applied for clutter with weak variations along the distance axis, as for example GPR system based coherent noise ringing, ground bounce and soil roughness scattering. For time synchronous artefacts, a background-removal is effective in allowing weaker or deeper events to become visible in a processed section. However, a drawback of this filter is that it can also remove much of the signature of slowly undulating soil horizons and other near-surface features. Thus, this type of filter is often necessary, but should be avoided if shallow soil stratigraphic or structural mapping is an objective of the GPR survey. More sophisticated approaches are necessary, if the statistical properties of the clutter vary along the distance axis, due to subsurface scattering. For the elimination of incoherent clutter the use of an fk-filter is a good approach.

Topographic correction is an important processing step for survey areas that traverse irregular terrain. Therefore, elevation measurements should be made to account for the distortion in the radargram due to elevation changes along the profile. For minor surface variations, time-shifting data traces can largely compensate for topographic variations. Figure 4-2 illustrates the basic concept of a topographic correction, where a sub-horizontal interface lies at depth D beneath a horst of height h. The velocity of the first layer is known or estimated to be v. The uncorrected radargram is shown on the left side, which could lead to a false interpretation of the data. When the data are topographically corrected, the elevation data and the estimated velocity of the upper unit are used to pull up the traces acquired over the horst structure by an amount $\Delta t=2h/v$. After the topographic correction, a geologically reliable interpretation of a flat reflector can be made. Another possibility for a topographic correction is a time-to-depth conversion combined with a static correction applying the (x,z) values to the time-to-depth corrected data.

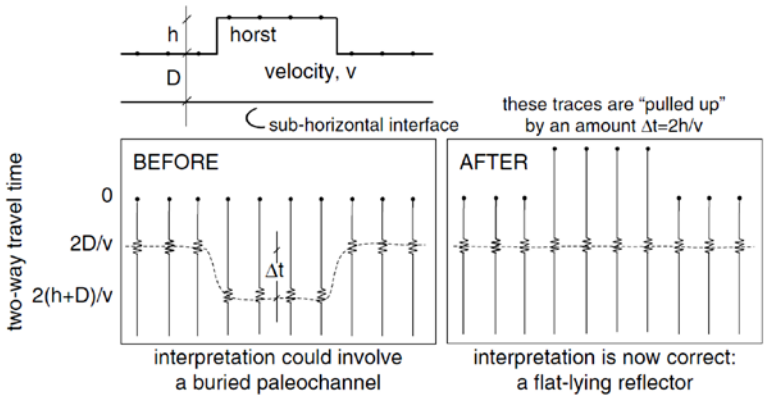

Figure 4-2: Simplified illustration of a GPR Topographic Correction (Everett 2013)

4.4 Velocity Analysis and depth estimation

The GPR data are recorded in the time domain with the depth axis of the radar section representing the two-way travel time (TWT). In order to convert the TWT values to correct depth values, the subsurface velocities along the profile must be known. Therefore, a CMP analysis can be performed by symmetrically expanding the TX and RX antennas about a common midpoint. The CMP velocity analysis is carried out in areas with flat-lying reflectors. For the case of heterogeneous subsurface conditions with point-like targets, the velocity can be estimated by fitting a hyperbolic function to the observed diffractions in the radar time section (Persico 2014). A point-like target can be a buried object small with respect to the minimum wavelength involved in the subsurface. The transmitter illuminates the target from a certain distance before and beyond it, as illustrated in Figure 4-3. Therefore, the receiver gathers echoes within a segment

centered on the target. The length of this segment is dependent on the directivity of the antenna, the characteristics of the subsurface and the depth of the target.

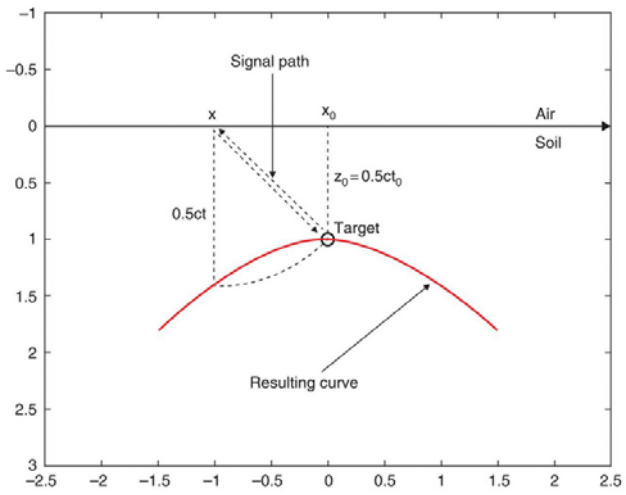

Figure 4-3: Measure of the EM velocity of the soil from a diffraction hyperbola from a point-like target (Persico 2014)

If the offset between transmitter and receiver can be neglected, the point target in the x-z domain is represented as a hyperbola in the x-t domain. The distance between the source-observation point (x,0) and the buried target (x_0,z_0) is defined by

$$d = \sqrt{(x - x_0)^2 + z_0^{\,2}} \tag{4-8}$$

and corresponds to the apparent depth, which in terms of propagation velocity is given by z(x)=vt/2, where t=t(x) is the return time of the echo recorded at position x.

$$t = \frac{2}{v}\sqrt{(x - x_0)^2 + z_0^{\,2}} \tag{4-9}$$

In the point $x=x_0$, the apparent depth of the target reaches its minimum value with the minimum recorded return time t_0. Equation 4-10 is parametric with respect to the propagation velocity v and thus, v can be estimated by fitting a diffraction hyperbola to the observed data. There are tools in commercial software packages that allow us to do this fitting in an immediate graphical way. Once the subsurface radar velocity is known, a *time-to-depth conversion* can be performed in order to display the reflection horizons at their actual depth beneath the surface.

5 Modelling of GPR Data

A way to understand the physical nature of a radargram is to simulate the system behaviour from the excitation through to the response that would be observed or measured. Modelling enables quantitative predictions of subsurface structures leading to a sound basis for interpretation. The main components required to build a GPR model include the design of measuring instruments and the theory of electromagnetic wave propagation. Modelling helps to find the exact processing strategy to extract important information and predict sensitivity to parameter changes. The block diagram from Figure 5-1 shows the general principles of GPR forward modelling.

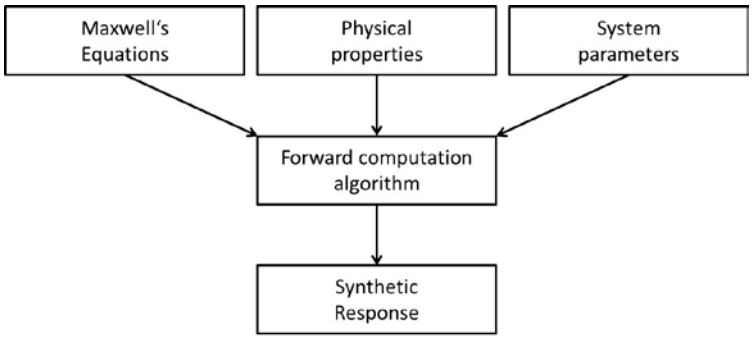

Figure 5-1: GPR forward modelling algorithm showing the main components for the computation of a synthetic radargram (Butler 2005)

5.1 Basics of GPR modelling with REFLEXW

Modelling has been examined within the modelling tool of the software REFLEXW (© K. J. Sandmeier), constructed for the processing and interpretation of GPR and seismic data. It allows the production of a 2-dimensional layer model and the simulation of electromagnetic wave propagation by means of finite difference (FD) methods, solving Maxwell's equations in a discretized area. A model is defined with start and end coordinates in x- and z-direction [m] and a number of different layers. Each layer has to be assigned a geometry in (x,z) and a set of electromagnetic values (relative permittivity ε [ ], effective magnetic permittivity μ [ ] and electric conductivity σ [S/m]) which can vary laterally. It is possible to model discontinuities of the subsurface by adding elements of different electrical values and shapes (circles, rectangles, triangles or lenses). The parameters necessary for the FD-computation are given in Table …The input frequency [MHz] shows the center frequency of the antenna to be modelled and the time window specifies the point of time in [ns] at which the simulation shall be terminated. The specification of the trace increment and time increment is based on the minimal wavelength and

the velocity and should not be overpassed to avoid numerical dispersion. As signal type a Kuepper wavelet and as source type an exploding reflector model have been selected. The exploding reflector model allows the simulation of a zero-offset-section in a single FD-simulation. Thus, all points stemming from a reflector are the starting point of a Huygen's elementary wave with an amplitude proportional to the reflexion coefficient for the normal incidence case (as described in section 3.1.3). A major difference between computational models and the real subsurface is the limitation of the model in space, thus unintentional reflections from the model boundaries occur. To avoid this effect, the model boundaries can be extended by an absorbing edge area (linear absorbing range). The result of this calculation are the x-, y-, z-components of the electrical and magnetic field depending on x, z and t.

5.2 Modelling Procedure

The modelling procedure carried out in this thesis is presented in Figure 5-2 and demonstrates the work flow of how to perform the numerical modelling of GPR data. The raw data are analysed using REFLEXW software applying standard filter routines. The propagation velocity of different subsurface layers is derived from diffraction hyperbola analysis and interfaces are picked by following phases with high amplitudes. A mean velocity is assigned to each layer and the layer model is converted from the time to the depth domain. If no velocity information is available from CMP measurements or diffraction hyperbola analysis, velocity-values can be based on borehole information and reference values from literature.

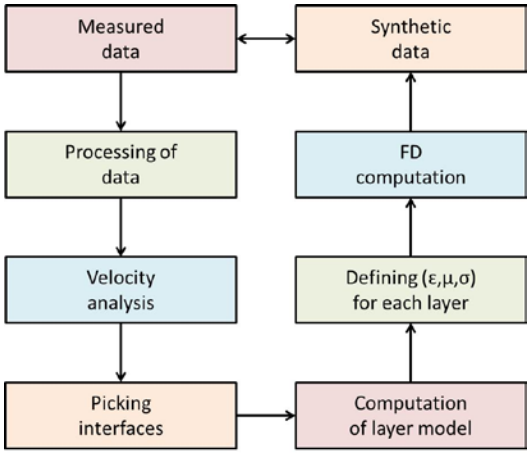

Figure 5-2: GPR Modelling procedure for GPR data with available diffraction hyperbolae information within the radargram.

In a second step, the layer model is imported in the modelling environment of REFLEXW, where electrical parameters can be assigned to the different model layers. As the reflection of GPR signals is related solely to variations in the electrical permittivity (ε) and conductivity (σ) of

the medium, variations of those parameters, and the geometry of the interfaces, in the numerical models could permit us to adjust the synthetic radargram to reproduce the actual measured data. Therefore, electrical permittivity values are calculated for each layer from the velocity values and conductivity values are retrieved from ERT inversion results. In the end, the synthetic radargrams should reproduce the patterns observed in the measured data.

5.3 Theoretical Models for layered media

In this section models with different settings are tested to better understand the propagation of radar waves in the subsurface. The first scenario which is numerically modelled is the GPR response for a horizontally layered model whose electrical permittivity values vary from layer to layer. The model presented in Figure 5-3 is composed of three layers (air, soil-A, soil-B), whereby soil-B exhibits laterally varying permittivity values.

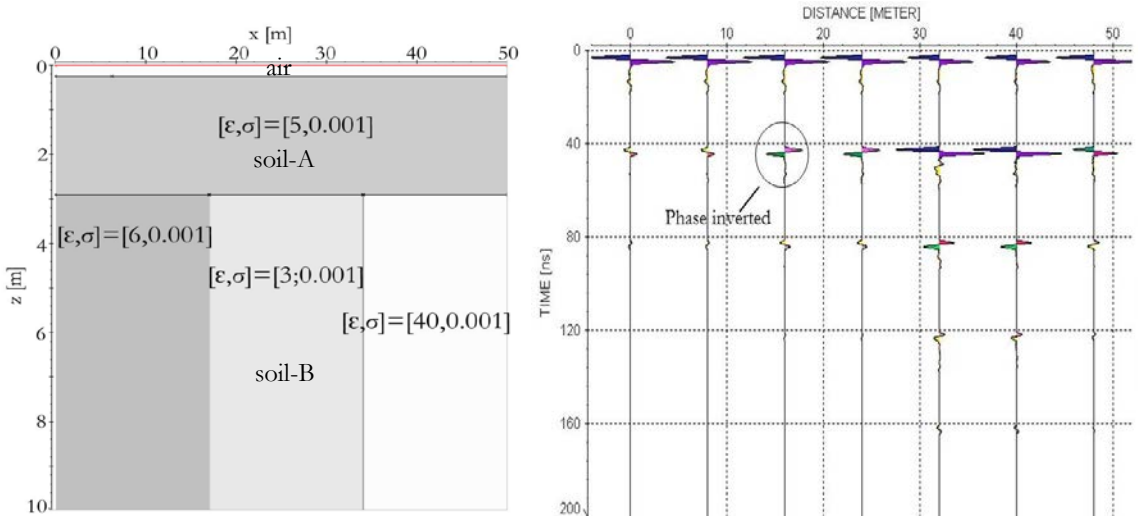

Figure 5-3: GPR simulation for modelling response of different permittivity values; left: Model of the subsurface with three layers (air, soil-A, soil-B) and laterally varying permittivity values in soil-B, right: synthetic model of the subsurface where three different reflection amplitudes and types are observed.

The synthetic radargram is displayed in wigglemode with a resampled trace increment of 10 meters. The reflection amplitude of the air-soil interface is high and has a negative polarity, as the wave is travelling from a medium of low electrical permittivity to a medium of higher electrical permittivity. The reflected pulses at ~40 ns correspond to the permittivity boundary of soil-A and soil-B. The reflections of the left part of the interface are weak since the contrast in the electrical permittivity values between the two soils ($\varepsilon_{soil\text{-}A}$=5, $\varepsilon_{soil\text{-}B}$=6) is small. In the middle part the reflection amplitude is higher, as the contrast between $\varepsilon_{soil\text{-}A}$=5 and $\varepsilon_{soil\text{-}B}$=3 is larger. Note that the two reflections of the middle part appear inverted w. r. t. the ground wave, because the wave is travelling from a medium of high impedance to a medium of lower impedance. The reflection off the right part of soil-B is largest since the electrical contrast is high. Additional phenomena

observed in this simulation are multiple reflections, where the wave is reflected at the (ε_{soil-A}- ε_{soil-B}) interface, returns back to the air-ground interface, reflects there, travels downward again and reflects a third time to be recorded back at the receiving antenna. These kinds of reflections lead to potential interpretation pitfalls of pseudo interfaces and have to be considered for high contrasts between two media. Direct multiples from the surface usually have twice the travel time of the primary reflecting energy.

In another example, the influence of the electrical conductivity on the reflected field strength is simulated and it is shown that reflections from electrical conductivity variations can be of the same order as those associated with electrical permittivity boundaries. Therefore, the electrical permittivity is kept constant for the two soil-layers and the electrical conductivity is laterally varied for soil-B. Figure 5-4 shows the synthetic radargram calculated for a 3-layer model with conductivity variations and uniform permittivity. For the conductive part (20m-50m) the reflection strength lies in the range observed in the last example.

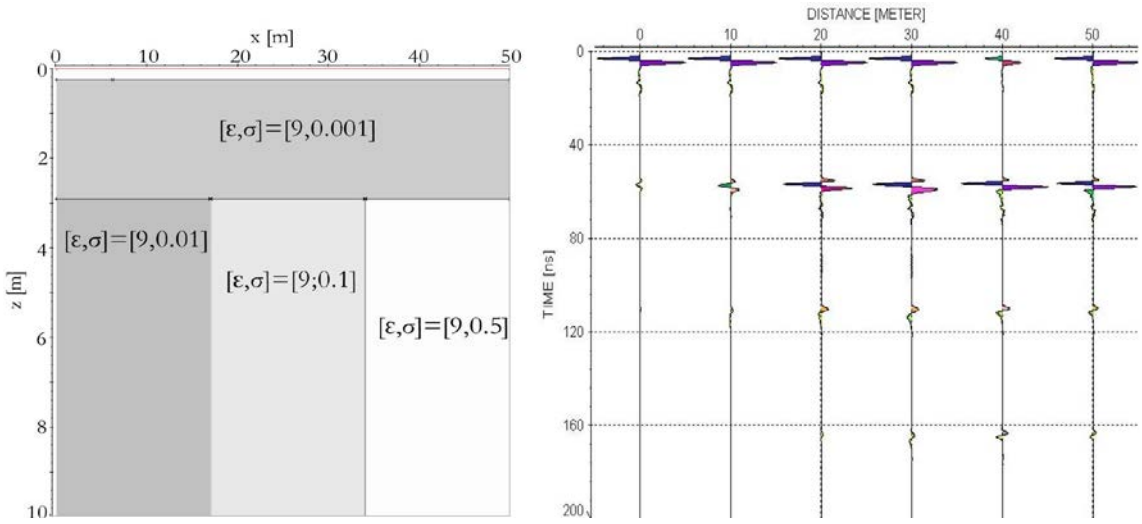

Figure 5-4: GPR simulation for modelling response of different conductivity boundaries; left: Model of the subsurface with three layers (air, soil-A, soil-B) and soil-B has laterally varying conductivity values, right: synthetic model of the subsurface where three different reflection amplitudes and types are observed.

In Figure 5-5 the attenuation of a GPR wave in a conductive medium is demonstrated. The higher the conductivity of the material, the faster the wave will dissipate into the ground, as described by Equation 3-9. Thus, features beneath conductive boundaries stay undetected. In this simulation, a conductive box (for example a copper box σ=5.8 S/m) is buried in a medium with laterally varying conductivities of 0.01, 0.1 and 0.5 S/m. The electrical permittivity is kept constant for the two layers to concentrate on the effect of the conductivity. The trace increment is increased to 0.5 m, to visualise the hyperbola arising from the copper box. Only in the left part of soil-B it is possible to detect the conductive box, because the losses in the background material

are small enough. Whereas in the middle and right part of soil-B the signal is completely attenuated and there is no information available about the depth of the buried box.

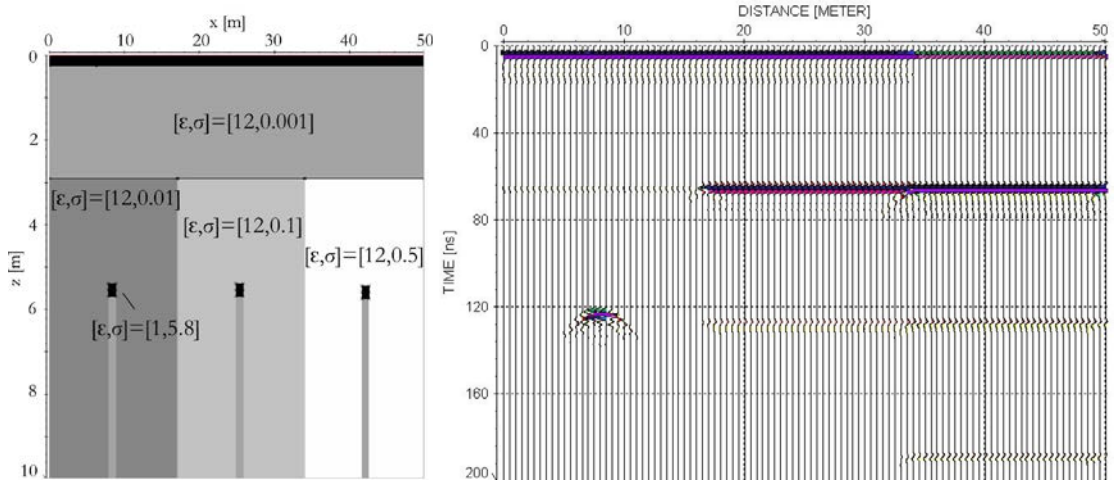

Figure 5-5: GPR simulation for modelling response of a high conductive box (for example a copper box) buried in media of different conductivity values; left: Model of the subsurface with three layers (air, soil-A, soil-B) and soil-B has laterally varying conductivity values, right: synthetic model of the subsurface where three different reflection amplitudes and types are observed.

6 Case Studies

In this chapter, three case studies are examined to test the modelling algorithm in different media (porous media and unconsolidated rock) and for several applications (landslides, contaminated sites). Considering the resistivity distribution in the subsurface as derived from ERT results and additional borehole information, diverse models are generated and synthetic data are compared to measured GPR data. Subsurface media consist of randomly distributed particles of different size and changing electrical properties. If the wavelength of the electromagnetic waves passing through the subsurface is comparable to the heterogeneities of the media, propagation of the wave is affected. To consider this effect, it is possible within REFLEXW to take the random distribution of these inhomogeneities into account, which is tested within the framework of the case study Wolfsegg.

6.1 Donau Island

The objective of the geophysical prospection at the Danube Island is a flood protection system for the danube in Vienna (Massinger and Michlmayr), where geophysical methods should help to characterise the subsurface conditions. Thus, within this context it was possible to examine different geophysical methods along one profile and construct a model of the electrical properties of the porous subsurface materials.

6.1.1 Study site and field work

The study area is located at the Donau Island, close to Floridsdorfer Brücke and the GPR measurements were conducted close to a borehole with 400 MHz, 200 MHz, 1.5 GHz and 40 MHz antennas. Additionally, Electromagnetic Induction, ERT and Transient Electromagnetic Imaging have been performed along the same profile and in the close proximity respectively.

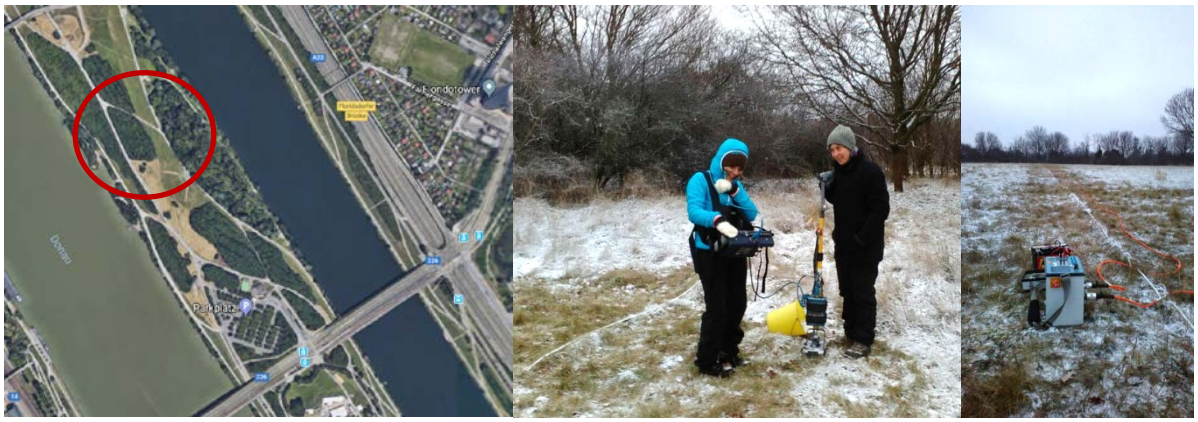

Figure 6-1: Study site Donauisland (left), GPR (middle), ERT measurements (right) along a 50m profile

Figure 6-2 shows the 70m long ERT profile with the 200 MHz GPR focus area marked, as the GPR data have been acquired from ERT profile meter 10 to 60. Borehole information is presented next to the ERT data.

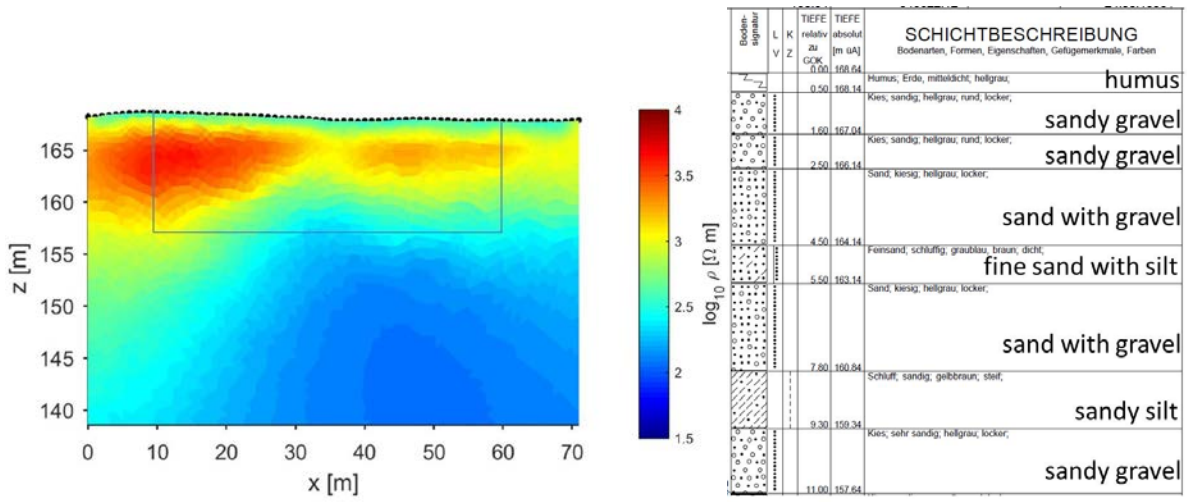

Figure 6-2: ERT profile with marked GPR focus area and borehole information

6.1.2 Results

The measured data are processed with a time-zero correction and presented in Figure 6-3. Both datasets show a first flat reflector at 18 ns and a second reflector at 50 ns which is slightly inclined. When comparing the measured GPR data to the ERT results, the geometry of the interfaces seem to be similar but stretched in depth.

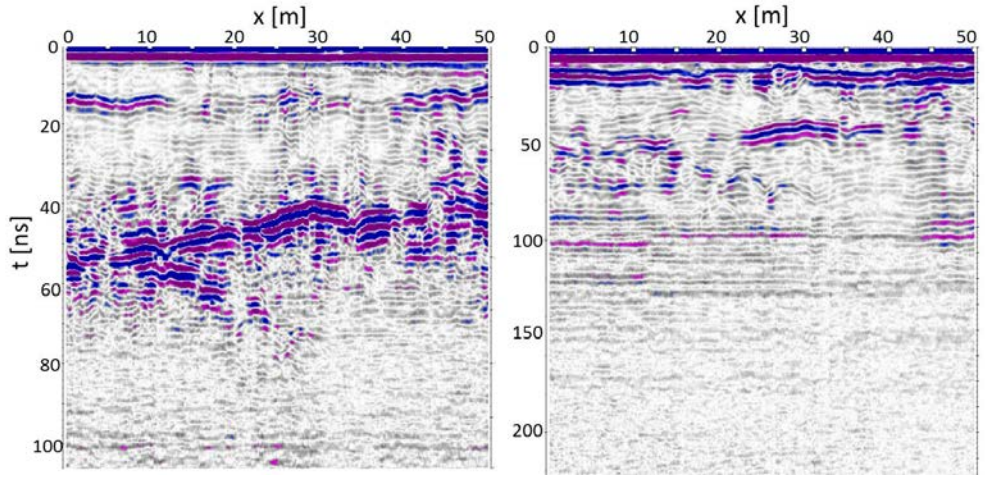

Figure 6-3: Measured GPR data using 400 MHz (left) and 200 MHz (right) applying time-zero correction, revealing two interfaces at 18ns and 50ns.

Therefore, modelling of GPR data is performed in order to reproduce the measured data. For the construction of the model, borehole information and standard permittivity values from literature define the depth and permittivity of the layers; whereas the conductivity values are retrieved from ERT results (see Figure 6-4). Thus, the two-dimensional model has a size of 50x10m, a frequency of 400 MHz, a time window of 100 ns, a discretization in space (trace increment for FD

computation) of 5 cm and in time (time increment for FD computation) of 0.24ns. It consists of a flat soil-layer exhibiting a high electrical permittivity over a slightly dipping gravel layer. Below the gravel, a wet sand layer with gravel is assumed which shows a high electrical permittivity value. The thickness of the sand layer will vary from two metres on the left margin to one metre on the right margin. Beneath the sand layer, a silt layer is recognized within the borehole information with high observed conductivity values of 0.02 S/m.

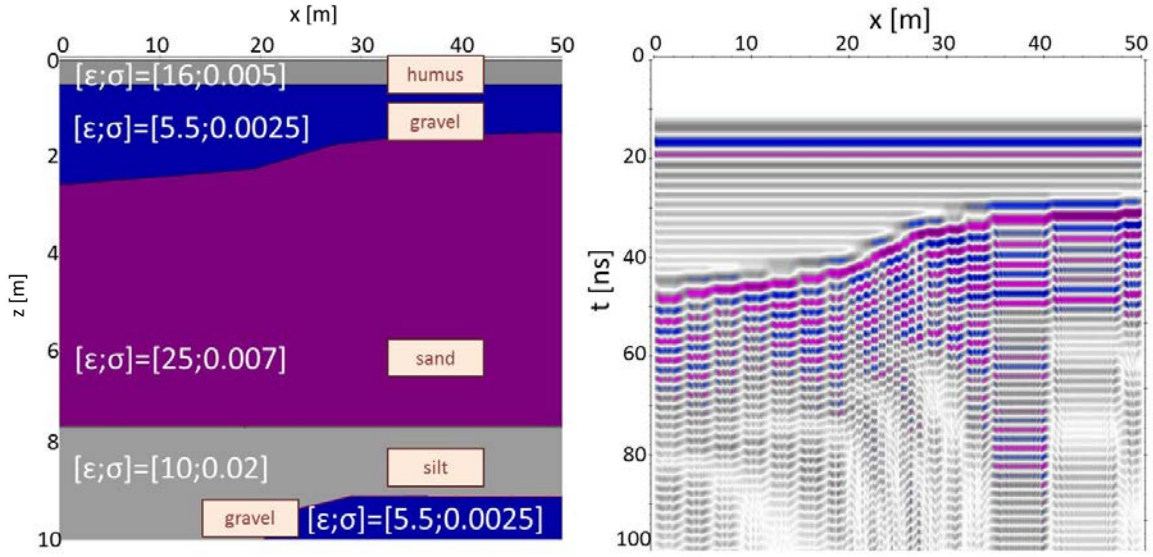

Figure 6-4: Basic 2-D model of the Donau Island subsurface and associated synthetic radargram

Depending on this information a synthetic radargram is calculated (Figure 6-4) and compared to the measured structures (Figure 6-3). Such plots reveal consistency and the possibility to derivate electrical properties based on the modelling of GPR signatures, borehole information and ERT results. The result shows two interfaces with high reflection strength, which are correlated with the humus-gravel interface and the gravel-sand interface. The reflected energy must be so strong that there is no energy available to travel down to the other two interfaces, thus no reflections are observed. A polarity change is noticed for both datasets, indicating a change from a high permittivity medium to a lower permittivity medium to a higher permittivity medium. Furthermore, the geometry of the dipping interface produces a reflection which is also observed in the measured data.

6.2 Wolfsegg

The geophysical investigation in Wolfsegg aims at characterising the subsurface as required to define the geometry of a recently developed landslide, quantify its internal structure and volume and delineate the hydrogeological settings. The combined application of EMI mapping, induced polarisation (IP) surveys, seismic refraction tomography (SRT), TEM surveying and GPR should

help to solve for a quasi-continuous 3D subsurface model. Besides the combined interpretation of the geophysical results and the borehole data, the structural information obtained through GPR is used to constrain the IP imaging results. Therefore, synthetic modelling of GPR data was performed to obtain a model of the subsurface structures.

6.2.1 Study site and data base

The study site is situated in an urban settlement in Upper Austria and features layers of coal/lignite, gravelly sands, sandstones and clays. The gridlines of the geophysical measurements are demonstrated in Figure 6-5 indicating the 160 m long GPR profile measured with a 200 MHz antenna.

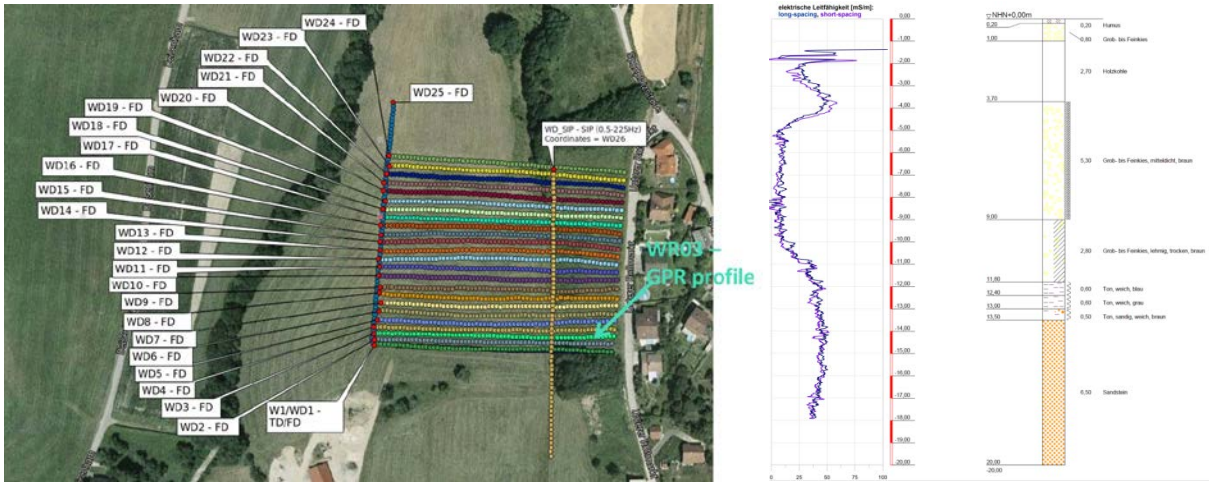

Figure 6-5: Study area Wolfsegg showing the grid of the geophysical investigations and the selected GPR profile for processing and modelling

Along the GPR profile, geoelectrical and TEM measurements have been conducted and borehole information is available. The borehole data consist of electrical conductivity measurements and lithological information.

6.2.2 Results

The GPR raw data are processed applying the following processing steps: time zero correction, bandpass filter, background removal, gain correction and a predictive deconvolution to filter out reverberations. In the end, a topographic correction is applied (see Figure 6-6).

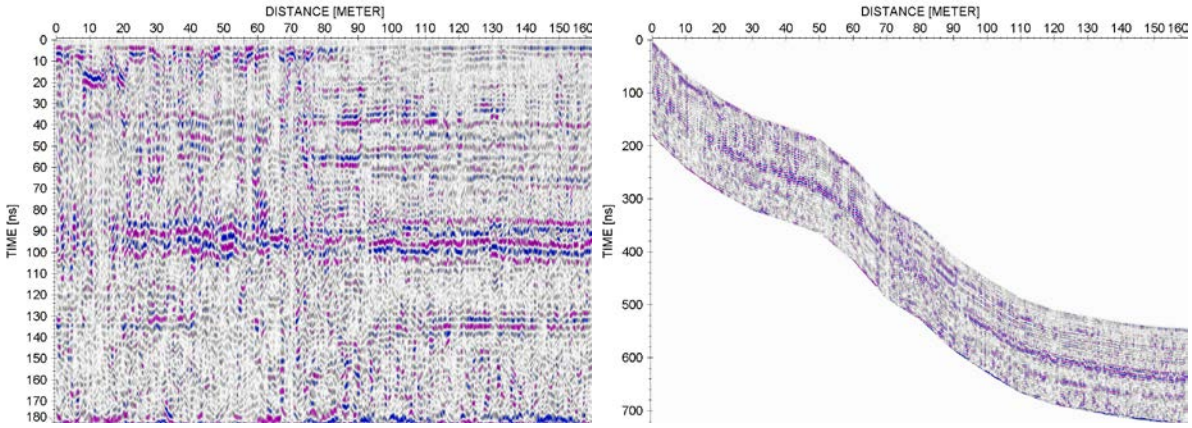

Figure 6-6: Processed data applying standard filter routines and predictive deconvolution (left) and topographic correction (right)

Interfaces are picked and mean velocities are assigned to each layer based on the lithological information and velocity values from literature. The picked layers are converted from time to depth and permittivity values are calculated from the velocity values. Electrical conductivity is retrieved from borehole data and assigned to the appropriate layers. The 2D – model in Figure 6-7 consists of 6 layers showing humus, coal, gravel and silt materials.

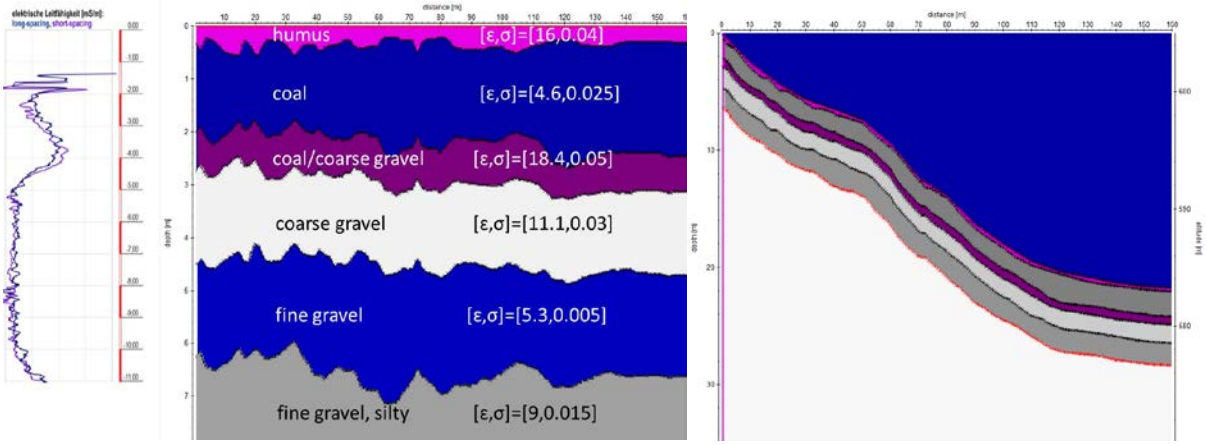

Figure 6-7: 2D-model of picked GPR subsurface structures with permittivity values from literature and conductivity values from borehole information and 2D-model with topography applied

The synthetic data show high reflection strength for the coal and coal/coarse gravel layer. In the same depth we observe an increase in the electrical conductivity, which could be associated with soil water. Multiple reflections are visible within layer 4 and layer 6, which could be falsely interpreted as additional interfaces. Thus, the interpreted interface from layer 3 to layer 4 could also be associated with a multiple reflection within the coarse gravel layer.

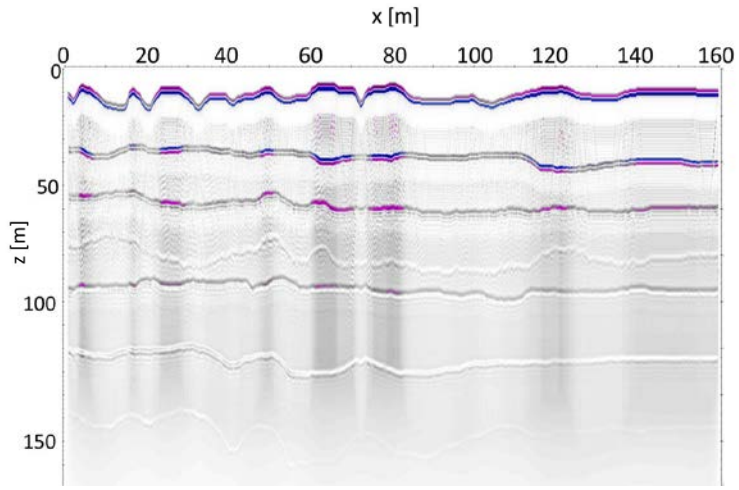

Figure 6-8: Synthetic radargram representing 6 layers and high reflection amplitude for coal and coal/coarse gravel layer.

To model inhomogeneities within soils, it is possible to add randomly distributed permittivity discontinuities. This can be realised by defining correlation lengths in x- and z-direction, a variance (which increases the range of epsilon, see Figure 6-9 (a) and (b)) and the fractional volume they take up in the medium (see Figure 6-9 (c)).

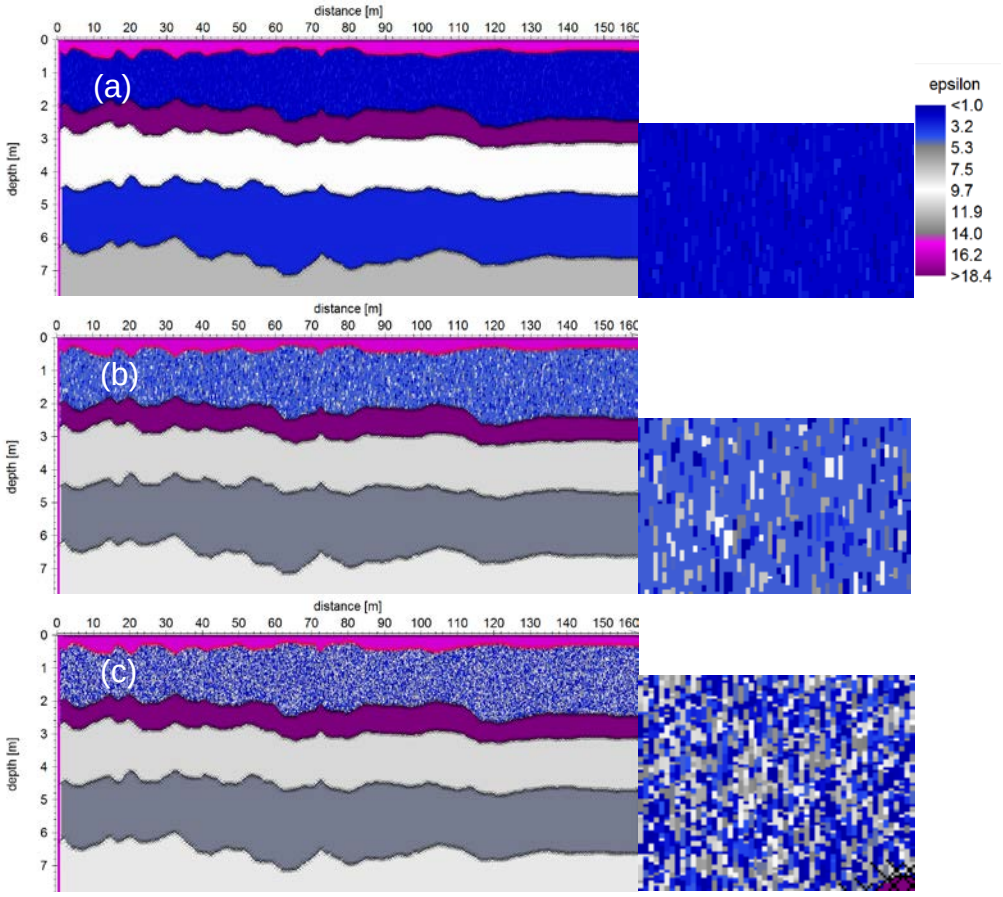

Figure 6-9: 2-D model with 6 layers and added discontinuities within the second layer with a correlation length in x of 0.5m and a correlation length in z of 0.3m and a (a) variance of 2, fractional volume of 10% (b) variance of 10, fractional volume of 10% and (c) variance of 10, fractional volume of 100%.

As for the case of Wolfsegg, the discontinuities are in the millimetre to centimetre range and the wavelength of the radar signal in the decimetre range, thus, wave propagation is not affected (see Figure 6-10).

layer	Corr. length x [m]	Corr. length z [m]	Var.	Dens. (%)
1	0.01	0.01	2	100
2	0.055	0.055	2	100
3	0.04	0.04	2	100
4	0.03	0.03	2	100
5	0.004	0.004	2	100
6	0.002	0.002	2	100

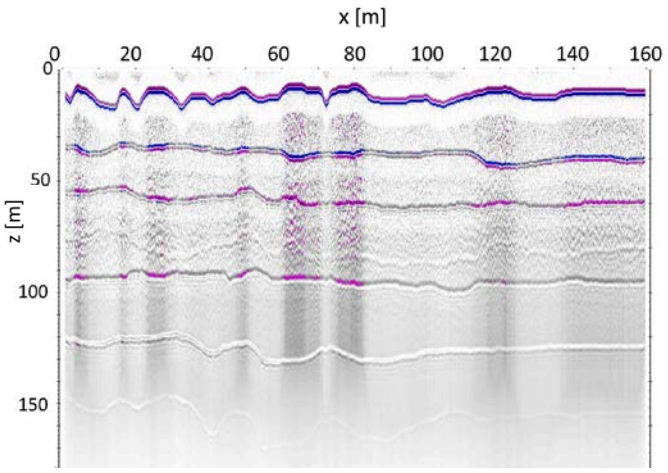

Figure 6-10: Discontinuities are assigned to each layer with correlation lengths in the millimetre and centimetre range, with a variance of 2 as epsilon variations should be in a small range (left) and associated synthetic radargram showing no change in the GPR response when compared to Figure 6-8.

Despite the modelling of GPR responses, a reliable 2D-model of the subsurface is difficult to achieve as the raw data show high signal to noise ratios limiting the ability to detect and discriminate soil horizons. Therefore, a revival of the measurements and a comparison among different frequencies could help to quantify measurement errors for a better detection of the subsurface features.

6.3 Stainach

The localisation and characterisation of the spatial extent of a contamination distribution in the subsurface of an area in Steinach is the issue of this case study. The contamination of the subsurface with tar causes a massif endangerment of the groundwater quality. The combination of geophysical methods (ERT, EMI and GPR) and borehole data should help at understanding the mechanisms of a contaminated site and quantifying the extent of the contaminant. Therefore it is necessary to provide a 2D-model of the electrical parameters of the subsurface at the study site.

6.3.1 Study site and data base

The contaminated area is located in Styria, close to the train station of Steinach/Irdning (Figure 6-11) and is characterised by sandy gravels, silt and clay materials. GPR measurements were

conducted within a grid near and in the contaminated zone with 200- and 400 MHz antennas. The 170 m long profile "st2" is further analysed using ERT inversion results and GPR modelling results.

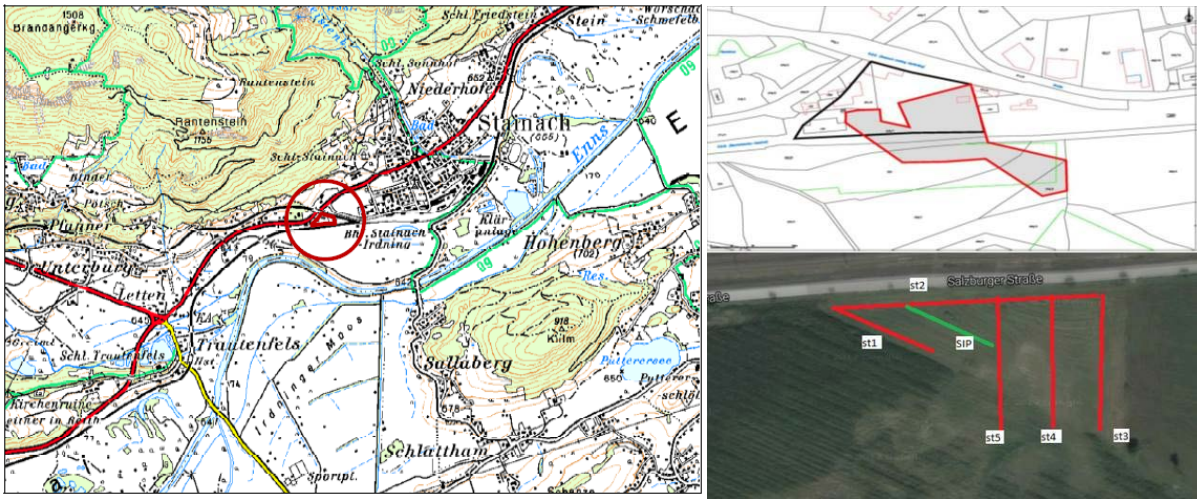

Figure 6-11: Contaminated area of geophysical investigations, the profile "st2" represents the GPR profile selected for modelling.

The resistivity values and borehole information indicate a first loamy soil layer showing low resistivities, followed by a sandy gravel layer with higher resistivity values (Figure 6-12). The third layer can be associated with silt and clay materials exhibiting, thus, low resistivities. Additionally, the profile clearly shows low resistivity anomalies revealed by the aged hydrocarbon associated with the development of porosity and mineral weathering due to carbonic and organic acids released by bacteria, as reported by (Flores-Orozco et al. 2012) Normally, for a contaminant high resistivities would be expected comparable with air or plastic. However, the microorganisms in the ground are feed by the contaminant and carbonic acids are released which show conductive behaviour. Due to the fact that aged hydrocarbons obtain higher density values, they are mostly located beneath the groundwater table, which is observed for profile meter 0 to 100.

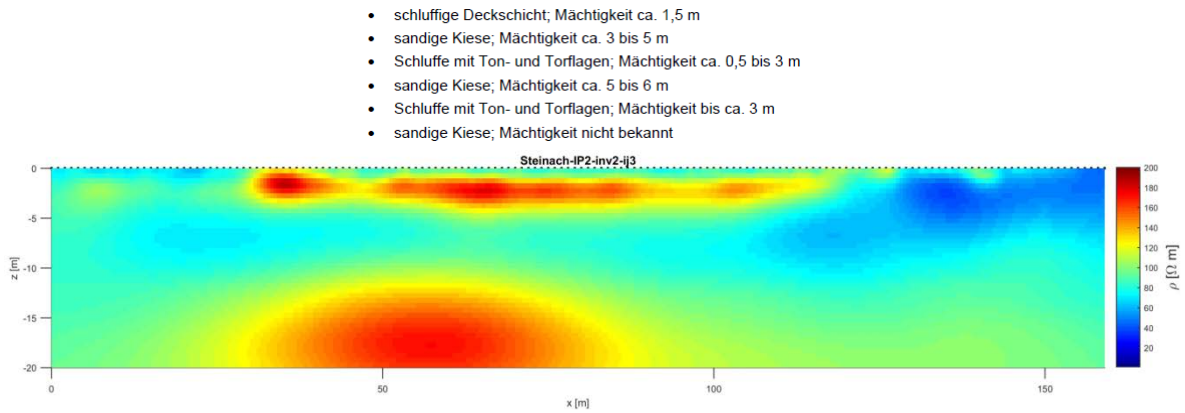

Figure 6-12: Lithological information of the site and resistivity distribution in the subsurface indicating sandy gravels, silts and clays and low resistivity anomalies associated with the contaminant plume

6.3.2 Results

Raw GPR data are processed applying standard filter routines and presented in Figure 6-13.

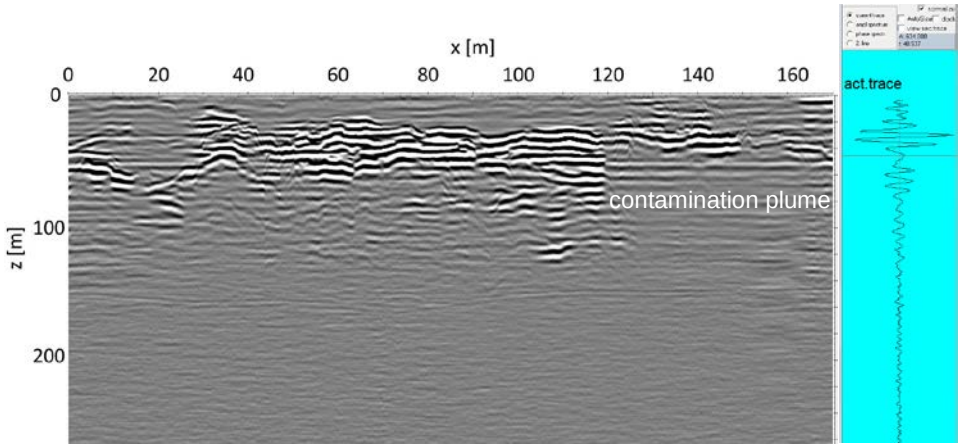

Figure 6-13: Processed radargram applying standard filter routines indicating the assumed location of the contamination plume and the phase change associated with the upper limit of the contaminant

The data quality is high and replicable, as the profile was measured twice and with different frequencies. A first layer with almost no reflections is observed in the processed radargram associated with the loamy layer described by resistivity and borehole data. Beneath this layer, an area (from 20 to 60 ns) of high reflection strength is identified representing the sandy gravel layer. The third layer is characterised by little reflections and is related to the silt/clay layer found by ERT and borehole information. The signal is attenuated within this layer, which decreases the penetration depth to ~120ns. Additionally, the GPR profile shows a zone of attenuated signals (from profile metre 120 to 170) beginning immediately below the interface from loamy soil to gravel extending to deeper depths and is similar to results of other GPR profiles within the contaminant zone. Microbial degradation causes changes in the chemical and physical properties of the contaminant and can thus change the electrical permittivity and the attenuation constant α (Atekwana and Atekwana 2010). As the electrical permittivity of contaminants and carbonic acids is smaller than the permittivity of sandy and saturated gravel, a phase change is observed indicating the upper limit of the contaminant (see Figure 6-13).

As a next step, layers are picked and velocity values are assigned to the appropriate layers based on values reported in literature. The velocities are converted to permitttivities and conductivity values are retrieved from ERT data. The simple 2D - model of the three subsurface layers and the calculated synthetic model are shown in Figure 6-14.

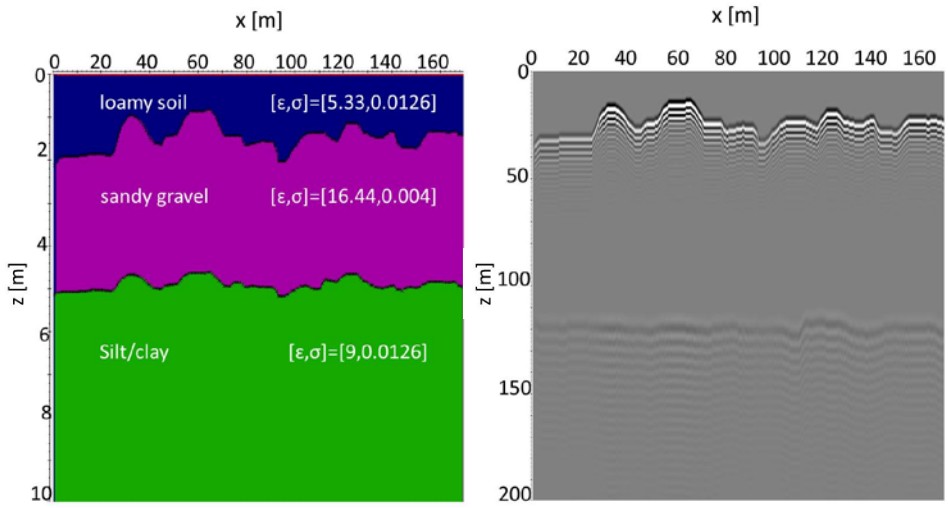

Figure 6-14: Model 1; simple 2D – model of three layers and synthetic model

The synthetic model shows a first interface with high reflection strength and a second interface with lower reflections. In order to model the contaminant in the subsurface, three rectangles are placed at the locations of low resistivity anomalies observed in the ERT data. In the first model, the rectangles are filled with air representing high resistivities and low permittivities simulating electrical behaviours of a contaminant (Figure 6-15).

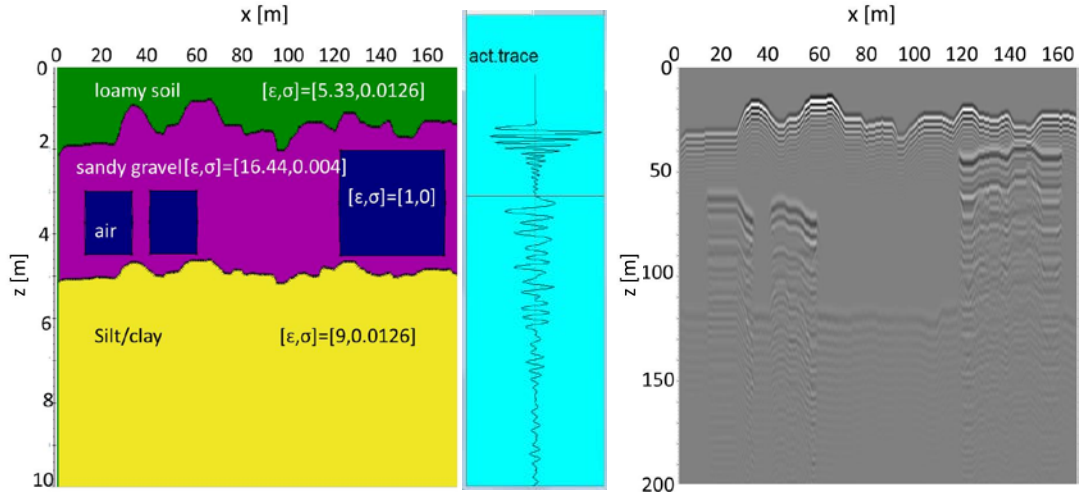

Figure 6-15: Model 2; three layer model with added rectangles filled with air and calculated synthetic model

The synthetic radargram calculated from model 2 shows high reflections from the surface of the rectangle extending to deeper depths. The same behaviour is observed for oil-filled rectangles. Both show a change in polarity which is due to the change in permittivity.

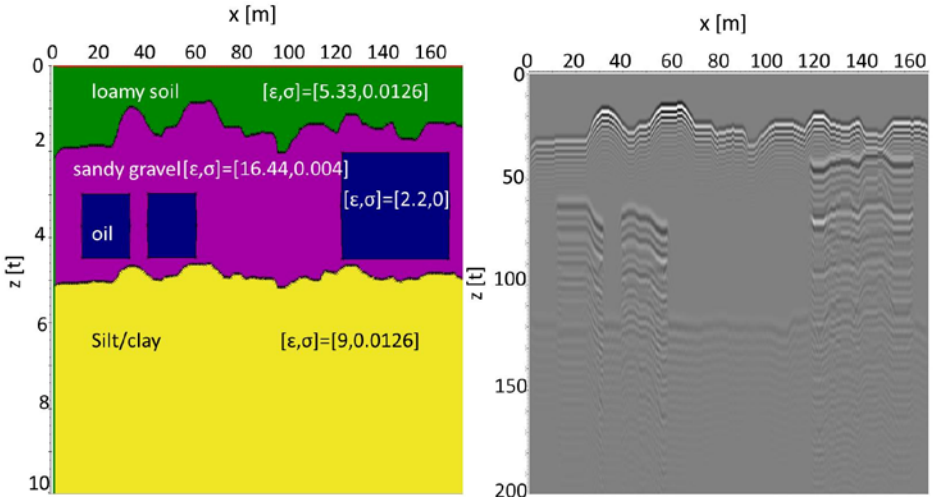

Figure 6-16: Model 3; three layer model with added rectangles filled with oil and calculated synthetic model

If the anomalies are simulated as carbonic acids with low permittivities and high conductivities, the synthetic data show a change in polarity (as in the case of air and oil) and attenuated signals below the upper limit of the anomaly (Figure 6-17). Thus, the interface to the silt/clay layer is not possible to identify due to the high conductivity and attenuation of the carbonic acids.

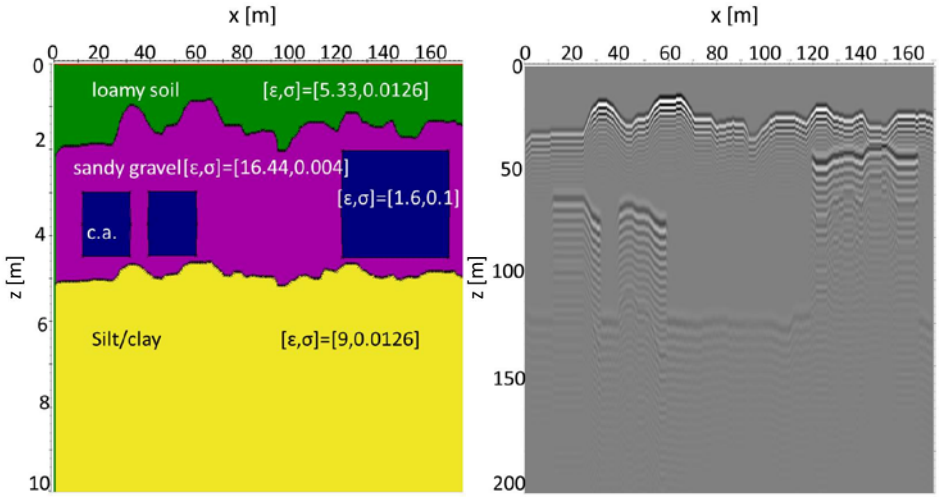

Figure 6-17: Model 3; three layer model with added rectangles filled with carbonic acids and calculated synthetic model

When comparing the synthetic data of model 3 to the measured data and ERT results (see Figure 6-18), important features can be reproduced and validated. From the synthetic data, it can be stated that the contaminant must extent over the entire profile length, as the interface to the clay/silt layer is not visible within the measured data. This could be simulated by defining a rectangle over the entire profile length. Another possibility to model this condition would be to pick the phase change observed in the processed data and define a layer/polygon representing the contaminant. Furthermore, it would be of utmost importance to evaluate and model the entire grid which has not been performed in this study.

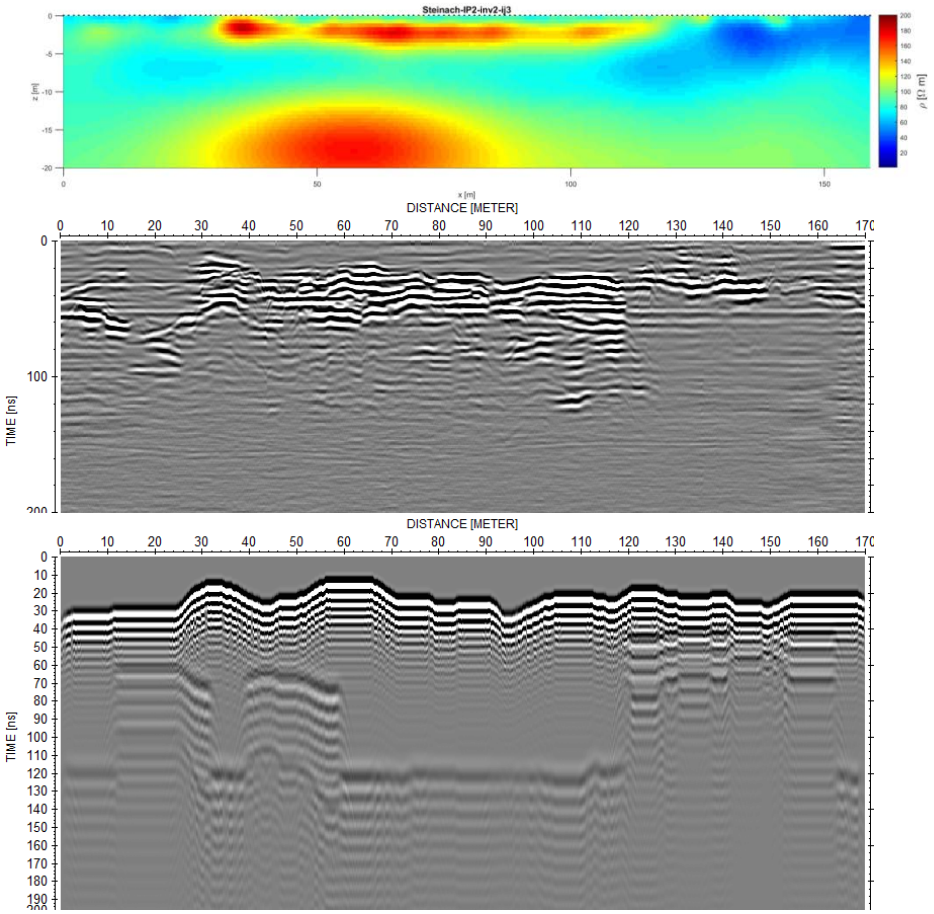

Figure 6-18: Comparison of ERT results, measured and modelled GPR data

7 Sonnblick

7.1 Study Area and Field Work

The study area is located on the south-facing slope of the summit of Hoher Sonnblick between the Sonnblick Observatory and the nearby glacier Goldbergkees, as demonstrated in Figure 7-1.

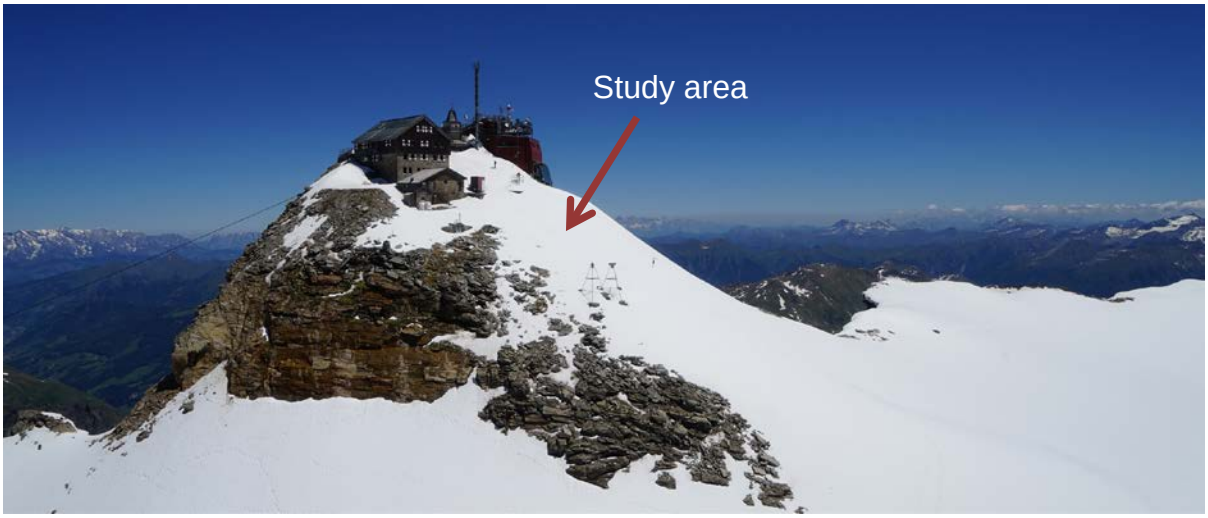

Figure 7-1: Study area of GPR measurements

A total of eight GPR measurement campaigns were organized between August 2015 and September 2017 (cf. Table 2). In those campaigns GPR datasets were collected using a SIR 3000 unit in a common offset configuration, mainly with 200 MHz and 400 MHz antennas, yet a few profiles were also collected with 80 MHz and 1.5 GHz antennas.

Table 7-1: Summary of all GPR measurements carried out at Hoher Sonnblick.

Season	*Date*	*Profile(s)*	*Measurement mode*	*Antenna frequency [MHz]*
Summer	02.08.2015 – 04.08.2015	Borehole, ERT	Continuous	400
Spring	07.06.2016	Borehole, ERT	Continuous	400
Summer	26.07.2016 – 28.07.2016	Borehole, ERT	Point	400
Summer	02.08.2016 – 04.08.2016	Borehole, raster	Point	200
Summer	30.08.2016 – 01.09.2016	Borehole	Point	200, 400
Autumn	31.10.2016 – 03.11.2016	Borehole, ERT	Point	200, 400, 1500
Spring	15.05.2017 – 19.05.2017	Borehole, raster	Continuous	80, 200, 400
Autumn	25.09.2017 – 26.09.2017	Borehole, ERT	Continuous	400

Since the active layer should be monitored, measurements were scheduled every three months to gain information about seasonal variations in subsurface properties, in particular the depth to

frozen materials. However, challenging weather conditions and the limited accessibility to the study area in windy conditions modified the scheduled measurements. Moreover, initial measurements in summer revealed poor data quality, as presented in Figure 7-2 (a) which compares a profile collected at Hoher Sonnblick in summer and in winter. This fact is likely associated to the rough surface conditions imposing changes in the velocity and trajectory of the GPR antennas due to stone blocks and plates, rock slides, etc.

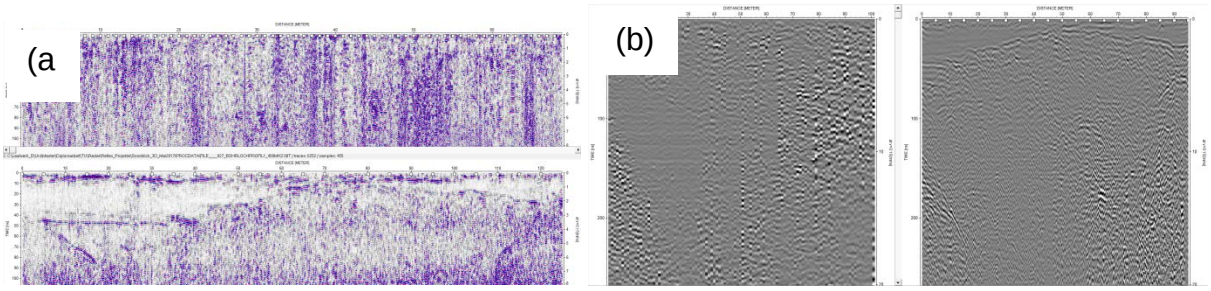

Figure 7-2: Measurements without (top) and with (bottom) snow cover (a) and comparison of point (left) vs. continuous (right) measurement mode (b)

Consequently, campaigns in 2016 were conducted as punctual measurements, which resulted in time-consuming surveys finally revealing only poor resolution (Figure 7-2 (b)). As a consequence, surveys were limited to winter conditions where the survey area was completely covered by snow, facilitating the continuous movement of the antennas. Therefore, the 200 MHz-antenna was equipped with a fix bent handle to facilitate the downhill measurements. This improvement of the measurement configuration resulted in a significant increase in the data quality and permitting to cover the entire study area for a characterization with higher resolution.

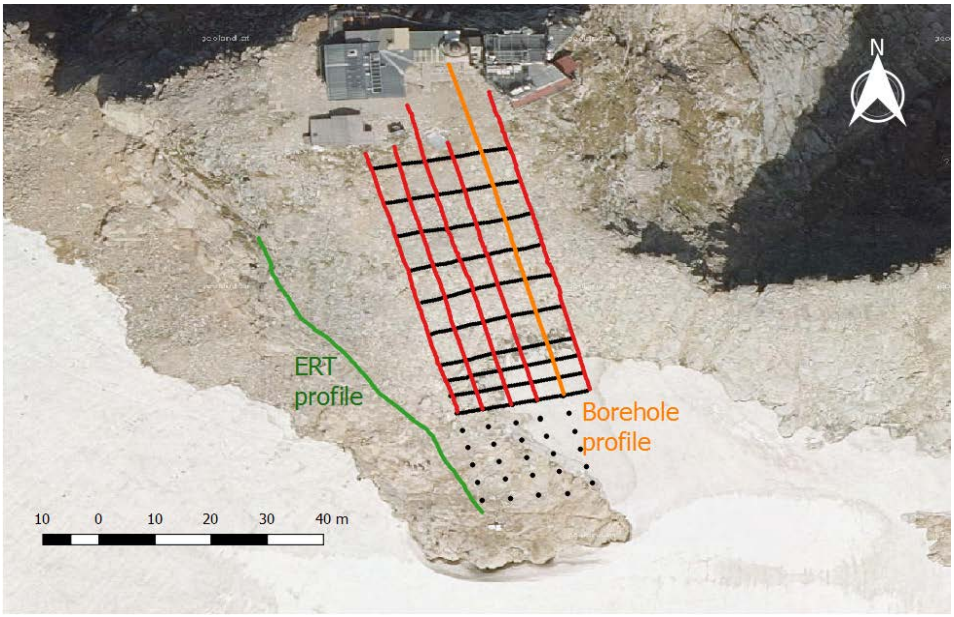

Figure 7-3: Orientation of the GPR profiles defined by six long profiles (red lines), 13 transverse profiles (black lines). The location of the ERT monitoring profile is indicated (green line)

An important step towards a 3D visualization of the active layer was the establishment and high precision differential GNSS (Global Satellite Navigation System) survey of a large-scale grid covering a vast part of the summit area in 2016, as depicted in Figure 7-3. The grid is composed of 5 long profiles (borehole profile and 4 parallel profiles) and 13 perpendicular shorter profiles yielding an area of ca. 20 x 120m. Using the high precision survey data, it was possible to stake out the grid (or parts of it) to repeat the measurements at the same location during all subsequent field activities. In 2017 the grid was extended towards the base station of the ERT monitoring profile of the Geologische Bundesanstalt (GBA), considering that information collected in 2016 revealed important features towards that direction.

Figure 7-4: left: Establishment of a large grid with a Differential GPS (Matthias Steiner), right: profiling with 200 MHz GPR antenna (Jakob Gallistl, Raphael Vasak)

GPR results presented here refer to a campaign in spring 2017 acquired along the gridlines using a 200 MHz antenna. A picture during GPR data acquisition is presented in Figure 7-4. The data were collected continuously with a trace increment of 2 cm and a time increment of 0.6 ns. To enhance data quality, a total of 32 stacks were required within a time window of 250 ns. Applying this measurement configuration, a vertical resolution of ~30 cm and a lateral resolution of ~60 cm can be expected for permafrost environment (Hauck & Kneisel, 2008) commonly related to electromagnetic velocities (v) of ~0.13 m/ns (at 1m depth).

7.2 Data Processing and Visualisation

GPR raw data are analysed using REFLEXW software applying the following processing steps discussed in Section 4.3.: Applying of the geometry (GPS-coordinates, marker interpolation), start time correction, bandpass filtering, gain correction and background removal. Because of the heterogeneous ground velocity, data migration has not been applied. The raw and processed data of an exemplary profile (borehole profile) are demonstrated in Figure 7-5.

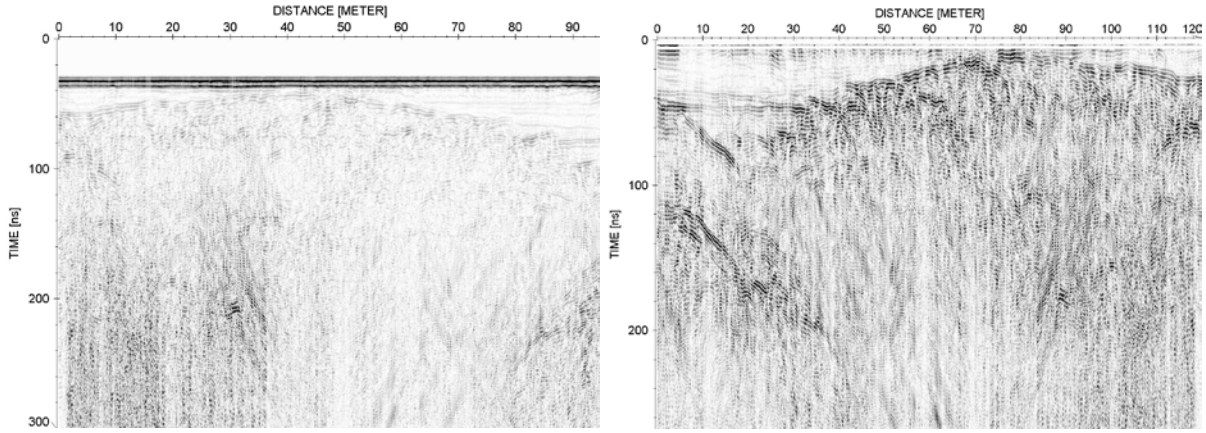

Figure 7-5: Raw borehole GPR profile measured with a 200 MHz antenna (left), processed borehole profile applying a geometry, start time correction, bandpass filtering, gain correction and background removal.

In all processed profiles noise with a certain dip (v = 0.2 m/ns) is recognized ranging from the surface to the deepest measured signal (Figure 7-6). Therefore, an f/k-filter is applied for the suppression of this kind of noise in the data. An f/k-spectrum is calculated which performs the Fourier transformation of the data range into the frequency-wavenumber domain.

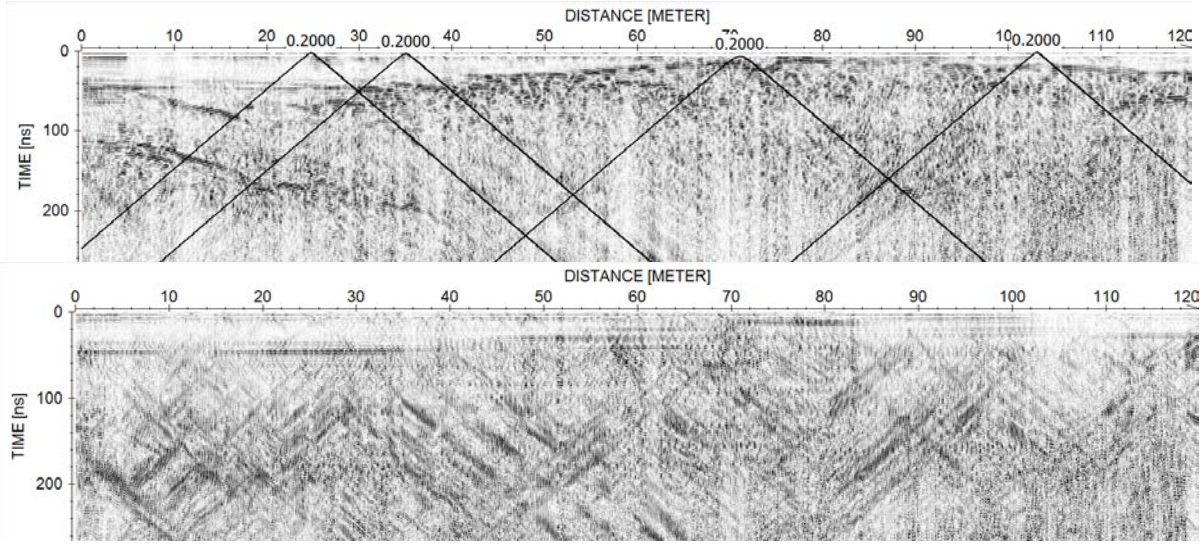

Figure 7-6: f/k filter applied to suppress the dipping events, top: processed radargrams revealing dipping events with a velocity of 0.2 m/ns (velocity of snow), bottom: noise which has to be filtered

By defining a velocity fan including the unwanted dip and applying a notch filter, the defined velocities are set to zero and the data are filtered according to Figure 7-7 representing the final processed and f/k – filtered data.

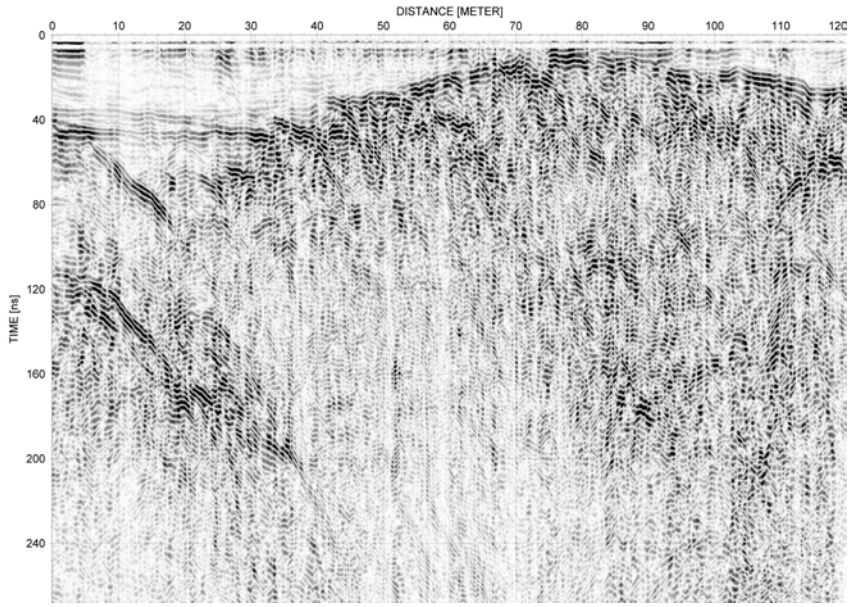

Figure 7-7: Final processed radargram, borehole profile

Now, the events with a dip of the velocity (v = 0.2 m/ns) are eliminated, but the question arises which impacting factor produces such events. A possible synthesis could be that water voids are present in the snow, as the data were collected in May where air temperatures start to rise. To validate this assumption, a simple model has been constructed representing a 4-layered earth. The first layer is associated to snow and water voids are added at the top of the snow layer. The resulting synthetic model exhibits the same dipping events as the measured data.

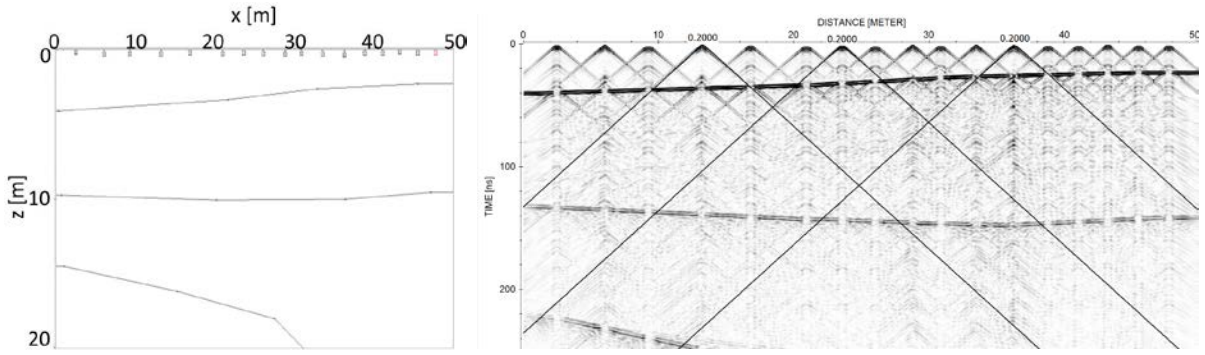

Figure 7-8: Modelling water voids in the snow within a 4-layer-model with the model of the subsurface (left) and the synthetic model revealing the same dipping events as in the measured data (right)

All measurements collected along profiles distributed in a regular grid as presented in Figure 7-3 are processed in the same way. In Figure 7-9, a comparison between two radargrams acquired along the same path with 400 and 200 MHz antennas is given. Both surveys were conducted in

spring, thus snow conditions are comparable. Additionally, similar features and lithological contacts are observed in both radargrams, discussed in the next section.

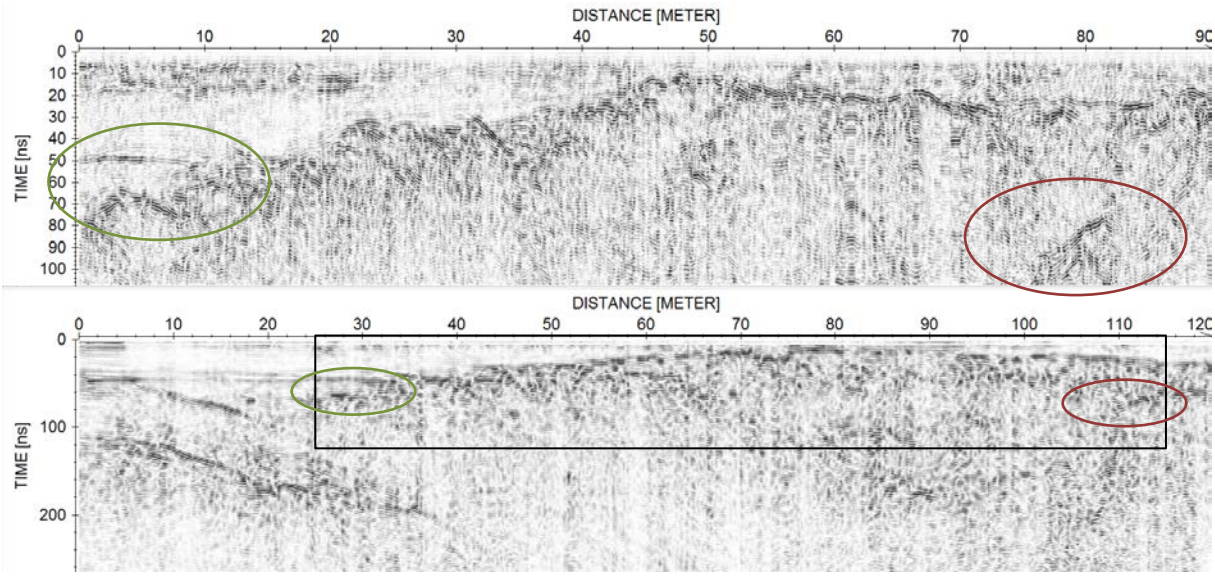

Figure 7-9: Borehole profile measured with two antennas; top: 400 MHz antenna, bottom: 200 MHz antenna, similar processing steps applied, ellipses of same colour mark similar features.

7.3 Velocity Analysis and Interpretation

Both radargrams from Figure 7-9 exhibit a similar pattern of reflections and a good match of the obtained velocity fields. The initial interpretation of the radargrams took into account amplitude information and the propagation velocity of the radar waves. Electromagnetic wave speeds of different media at the summit area of Hoher Sonnblick are estimated by measuring the curvature of the reflection hyperbolae in the radargram sections. The obtained velocities are superimposed on the exemplary profile (borehole profile), and interfaces are picked for materials with different electrical properties (Figure 7-10). The uppermost layer is characterised by almost no reflections and associated with the snow cover at the summit area with observed propagation velocities between 0.22 and 0.24 m/ns. Snow depth decreases with increasing profile meter and altitude. Beneath the snow layer the topography of the ground is clearly represented by the first strong reflector produced by reflections hinting at a boulder surface with voids (debris). Within this debris layer a dense diffraction pattern is observed revealing propagation velocities between 0.09 and 0.12 m/ns. Both antennas show a well-defined horizontal reflection at about 50 ns at the beginning of the profile just below the snow bottom. This feature is associated with the permanent snow field (firn) inducing velocities of 0.2 – 0.21 m/ns since old snow contains decreasing air volumes. As we know from glacier analysis of ZAMG, the glacier Goldbergkees is situated at the beginning of our grid (see Figure 7-3). Thus, the reflection at the bottom of the

firn material could be related to the glacier tongue, while the reflection beneath could be associated with glacier material (moraine). This assumption is supported by the detection of reflection hyperbolae with velocities between 0.16 – 0.17 m/ns, which demonstrates the velocity range for glacier ice. In the upper summit area, we observe velocities in the range of 0.13 and 0.16 m/ns at times between 80 and 250 ns, which are related to mountain permafrost. However, due to low SNRs from profile meter 80 to 120, it is difficult to delineate the depth to the permafrost body. Additionally, it is not clear whether the high reflection at the end of the profile (detected in both surveys with 400 and 200 MHz antennas) is related to bedrock permafrost or some other feature in the subsurface.

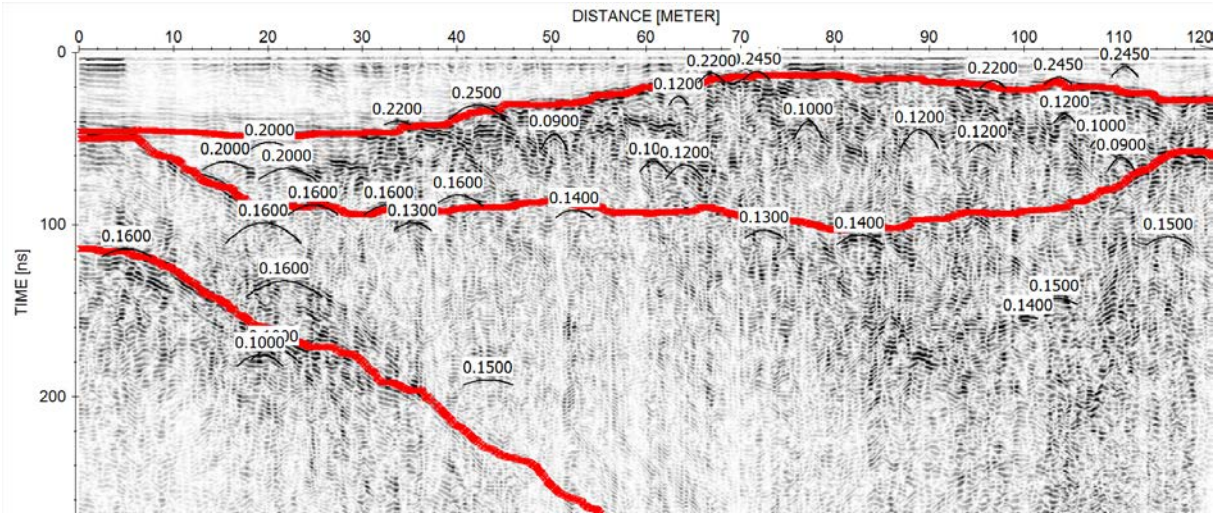

Figure 7-10: Interpretation of borehole profile measured with 200 MHz antenna, diffraction hyperbola show velocities for snow, firn, debris, ice and permafrost. Picked interfaces highlight the main horizons within the subsurface.

Therefore, modelling of electrical properties for the computation of synthetic radargrams was carried out to permit a better interpretation of the observed changes in GPR patterns. Interfaces are picked according to Figure 7-10 and mean layer velocities are assigned to the four layers to convert them from time to depth.

7.4 Modelling

For the construction of the numerical models in this study, the resulting velocity model is imported into the modelling environment of REFLEXW and electrical permittivity values for each layer are calculated from the velocity values. Conductivity values are retrieved from ERT inversion results. Figure 7-11 shows a first simple model of the subsurface at the summit of Hoher Sonnblick with four layers representing snow, debris cover, frozen jointed bedrock (mountain permafrost) and unconsolidated glacier material. The supposed firn and glacier is

ignored in this simple interpretation of the subsurface. The parameters for the FD computation are shown in the table right to the model of Figure 7-11.

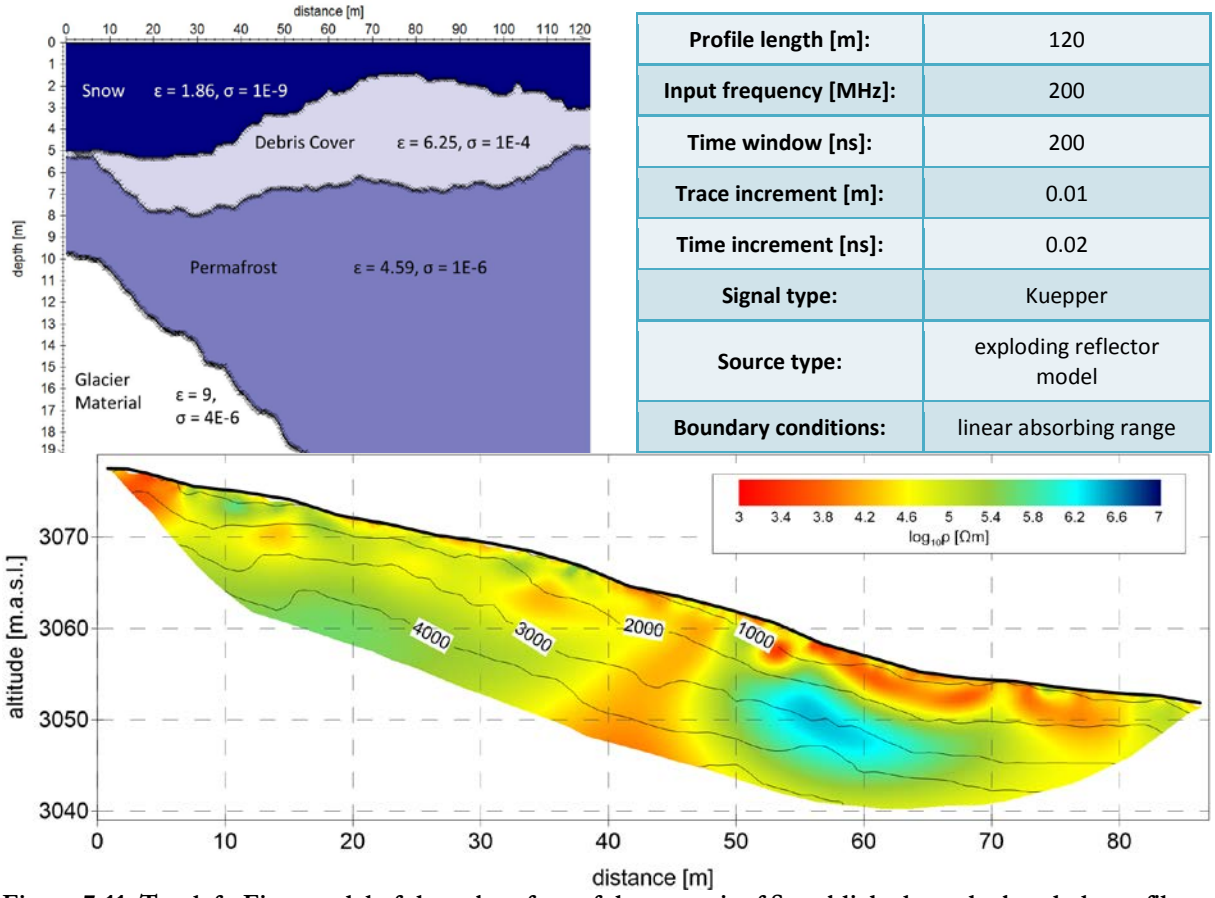

Profile length [m]:	120
Input frequency [MHz]:	200
Time window [ns]:	200
Trace increment [m]:	0.01
Time increment [ns]:	0.02
Signal type:	Kuepper
Source type:	exploding reflector model
Boundary conditions:	linear absorbing range

Figure 7-11: Top left: First model of the subsurface of the summit of Sonnblick along the borehole profile with four layers representing snow, debris cover, permafrost and glacier material; top right: Table of the parameters required for the FD computation; bottom: ERT profile representing the resistivity values of the subsurface at Hoher Sonnblick.

The calculated synthetic model is demonstrated with a new colour code in Figure 7-12 to demonstrate polarity changes. The result is characterised by a well-defined high-amplitude first reflector representing the interface between the snow cover and the ground surface, which is in good alignment with the measured data. However, in the first 30 metres the measured data show weaker amplitudes than the synthetic data, resulting in a smaller contrast in the permittivity values. This fact confirms the assumption of firn beneath the snow cover in the first 30 metres of the profile. The synthetic interface between debris and permafrost is characterised by generally weaker amplitudes and a change in polarity, whereas the measured data show the change in polarity only for profile metre 30 to 120 and high amplitudes for the first 30 metres. Additionally, the interface to the permafrost body in the measured data is only partly visible, which could be caused by the presence of air- or water-filled voids within the debris material (coarse blocks and boulders of different size). The glacier material is represented by high amplitudes for both synthetic and measured data.

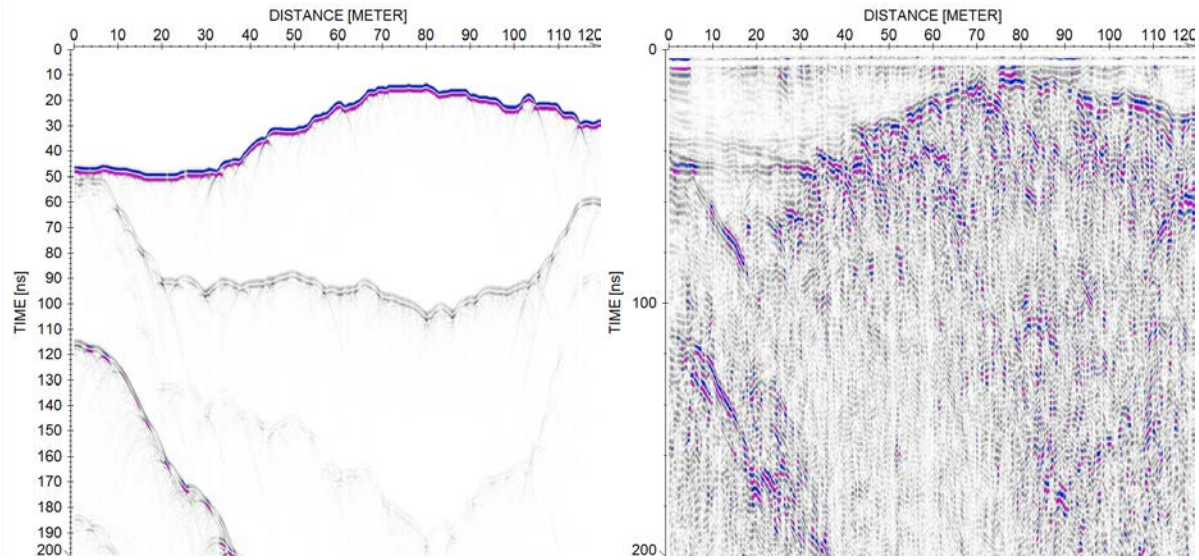

Figure 7-12: Comparison between synthetic radargram computed for the model demonstrated in Figure 7-11 (left) and processed measured data (right).

The interpretation and comparison of the synthetic and measured data helps us to adjust the model in a way to better reproduce the measured data. Therefore, water- and air-filled fractures are added to the second layer of the model from Figure 7-11, in order to match the patterns observed in the measured data. Moreover, lateral variations of medium properties are considered to reconstruct the firn and glacier ice beneath the snow cover in the first 30 metres of the profile. The adapted model is presented in Figure 7-13.

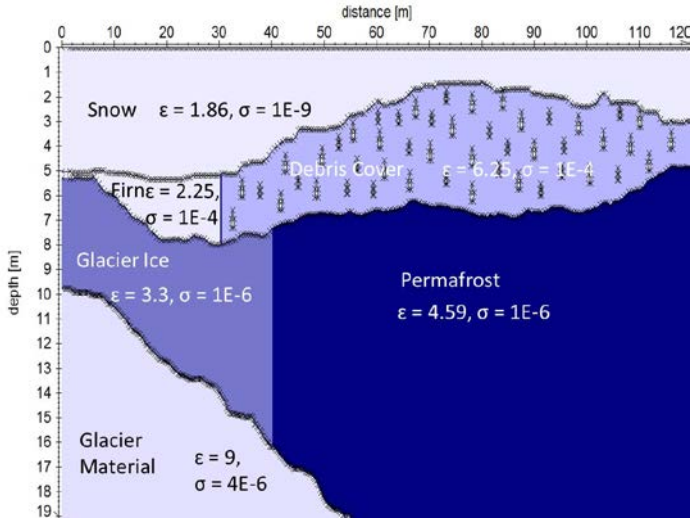

Figure 7-13: Adapted model with fractures added in the second layer representing the debris cover and lateral changes in the permittivity values indicating the glacier environment in the first ~30m of the profile

The resulting synthetic radargram is a good approximation of the real subsurface geometry, where the reflection strength observed for the first 30 metres reproduces the measured data. For both measured and synthetic data, the change in polarity from debris to permafrost is caused by the decrease in permittivity and the reduction in reflection amplitude is due to scattering of the radar waves within water filled voids in the debris cover.

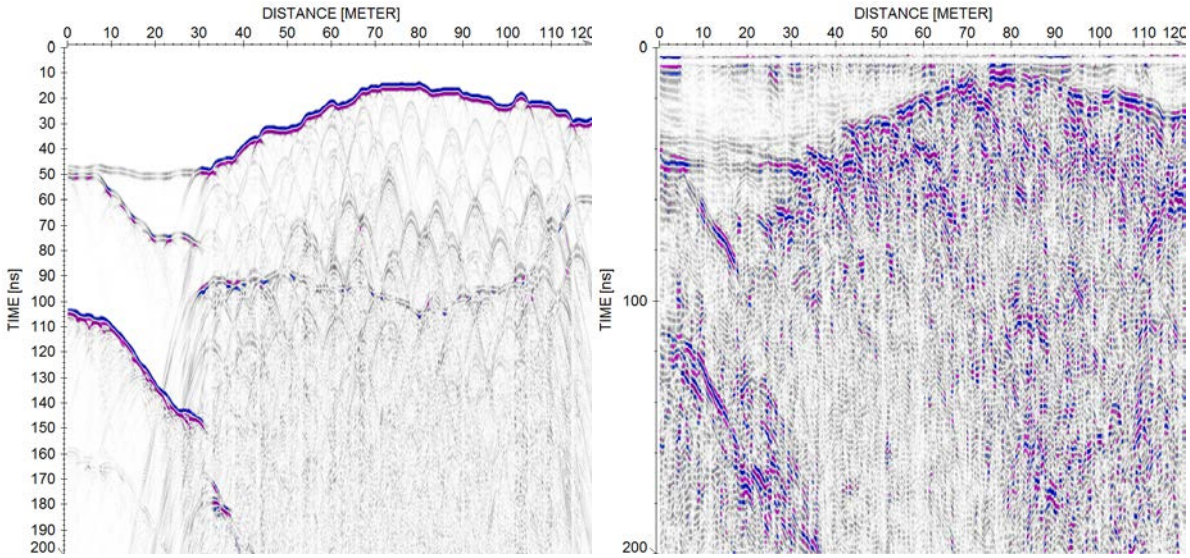

Figure 7-14: Synthetic radargram computed for the adapted model showing high reflection amplitudes for snow-ground interface, lower reflection amplitudes for snow-firn interface and high reflection amplitudes for glacier ice – glacier material interface and a change in polarity from debris to permafrost

There is still a doubt concerning the depth to the permafrost table at the end of the profile close to the Sonnblick observatory, where the depth to the permafrost body is decreasing. Because of the heat produced by the building, the permafrost table should at least stay at the same depth or even increase in depth. Therefore, the interface between the debris layer and the permafrost layer is picked again without considering the strong reflector observed in the last 10 profile meters which could also be related to constructions of the building containing metal. An exemplary model is shown in Figure 7-15, where the depth to the permafrost body in the last 20 metres is deeper and two pipes are added within the debris cover.

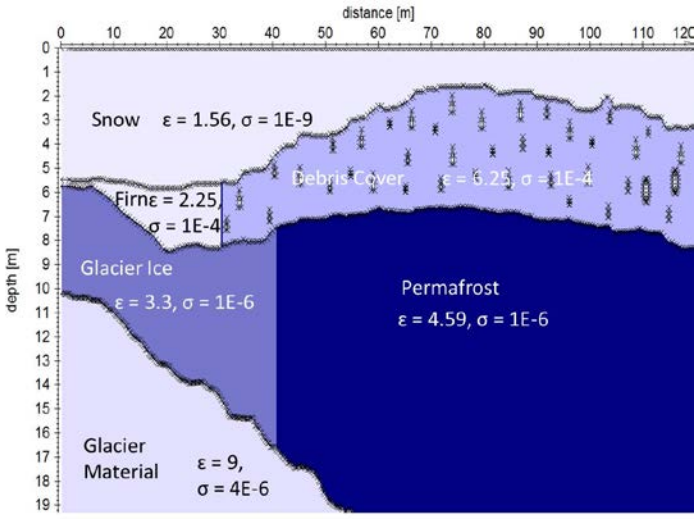

Figure 7-15: Improved model with a deeper permafrost table in the last 20 metres and two added pipes in the debris cover

The synthetic radargram proves that buried metal could be an appropriate explanation for the strong reflector observed in the end of the profile. Additionally, due to the low SNRs caused by

the debris cover in the uppermost area of the summit of Sonnblick, the depth to the permafrost table is not clearly delineable. Nonetheless, electrical modelling proved to be a helping tool to give an adequate approximation of the periglacial environment present at the summit of Hoher Sonnblick exemplified by Figure 7-16.

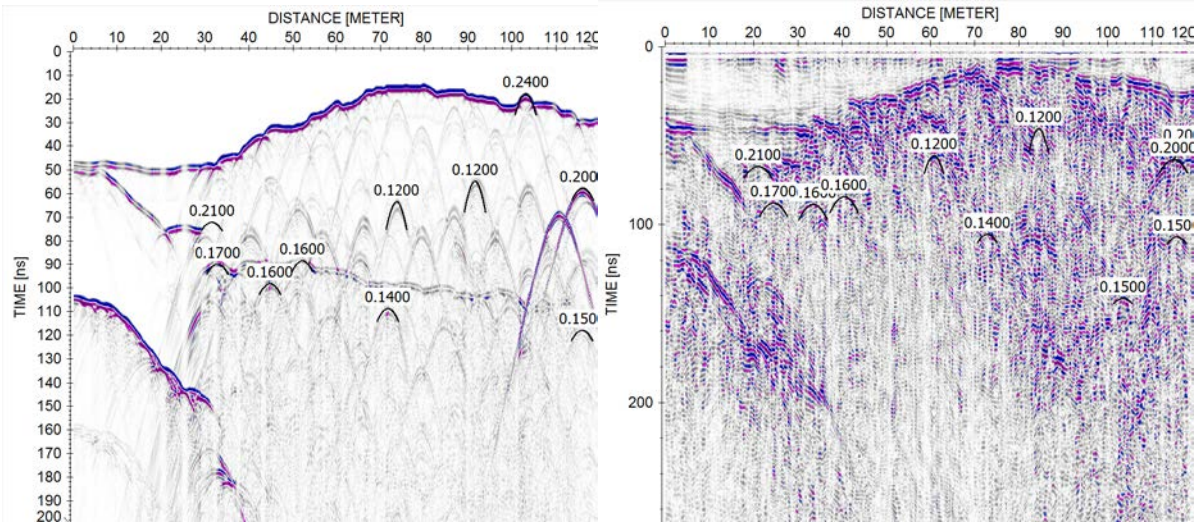

Figure 7-16: Exemplary synthetic radargram compared to the measured data with obtained velocities superimposed on the profile

The synthetic and measured data are converted from time to depth with the obtained velocity model and the topography is applied by a static correction (see Figure 7-17). For a uniform height reference, which is comparable for different surveys and projects, the xy-values obtained by DGPS surveys are used to extract the appropriate z-values from a 1m-elevation model. The snow depths obtained by the GPR are added to the height values representing the topography of the synthetic and measured data in Figure 7-17.

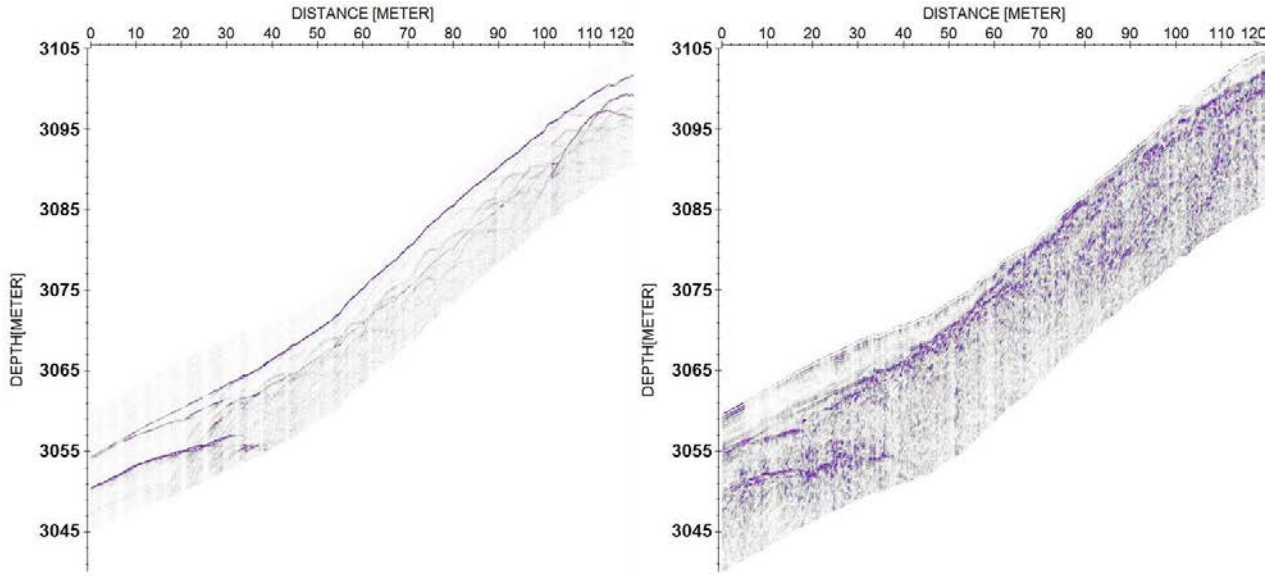

Figure 7-17: Topographic correction after an applied time to depth conversion for both synthetic and measured data, the topography is represented by z-values from elevation model and added snow depths

7.5 3D Model of the subsurface

The tests performed on several synthetic and field data sets (at different frequencies) allow a detailed analysis in order to obtain reliable results of the depth to the permafrost body within an area of ~100x20m. An appropriate model is generated for the four long profiles parallel to the borehole profile and the interfaces of each layer are interpolated within the software Surfer applying an inverse distance interpolation algorithm. The perpendicular profiles from Figure 7-3 are not considered in this interpolation, as the profiles collected within the upper summit area show low resolution making an identification of interfaces impossible (see Figure 7-18 top).

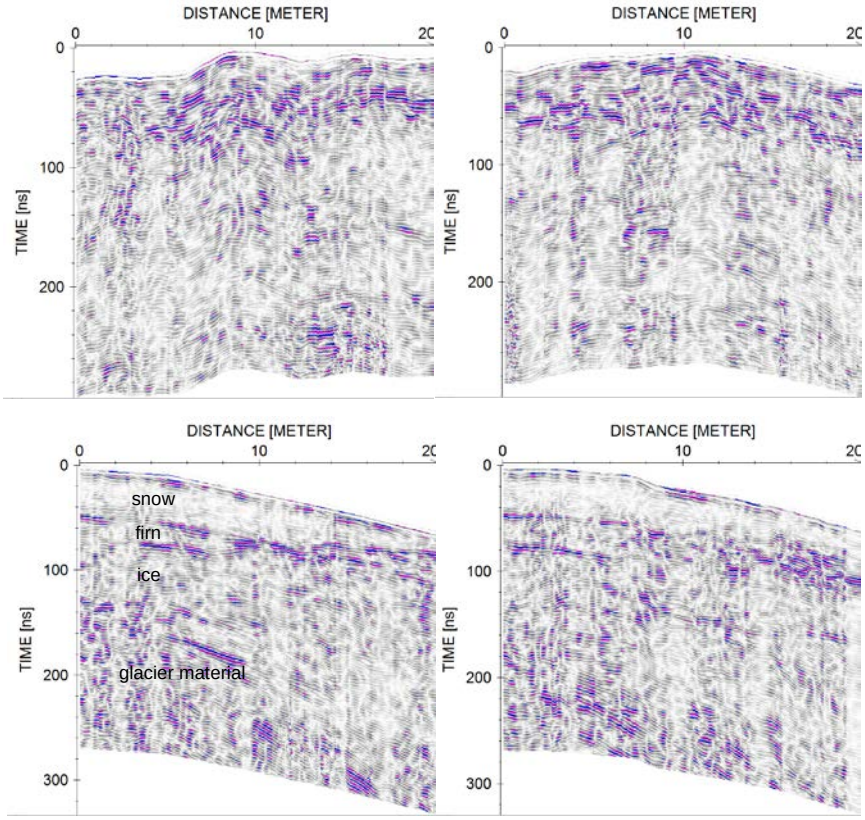

Figure 7-18: Examples for perpendicular profiles showing (top) two profiles from upper summit area with snow cover and attenuated signals within the debris cover and (bottom) two profiles from lower summit area with characterised snow cover, firn, ice and glacier material comparable with long profiles.

The two profiles from the upper summit area (Figure 7-18, top) are characterised by a layer of no reflections associated with the snow cover followed by a layer of high reflectivity representing the debris cover. Within this layer, the signal is attenuated due to water voids causing a higher conductivity (compared to first layer of ERT profile in Figure 7-11). The two profiles from the lower summit area (Figure 7-18, bottom) show similar features and depth values to the long profiles. Despite good accordance of the lower perpendicular profiles and the long profiles, the interpolation is restricted to the five long profiles to obtain consistent resolution within the

whole summit area. Further investigations should consider structural information from perpendicular profiles of the lower summit area to obtain a high resolution 3D model of the periglacial environment.

The generated raster is imported into the geoformation system QGIS and a contour plot is created illustrating the snow depth (see Figure 7-19) and the depth to the permafrost body (see Figure 7-20).

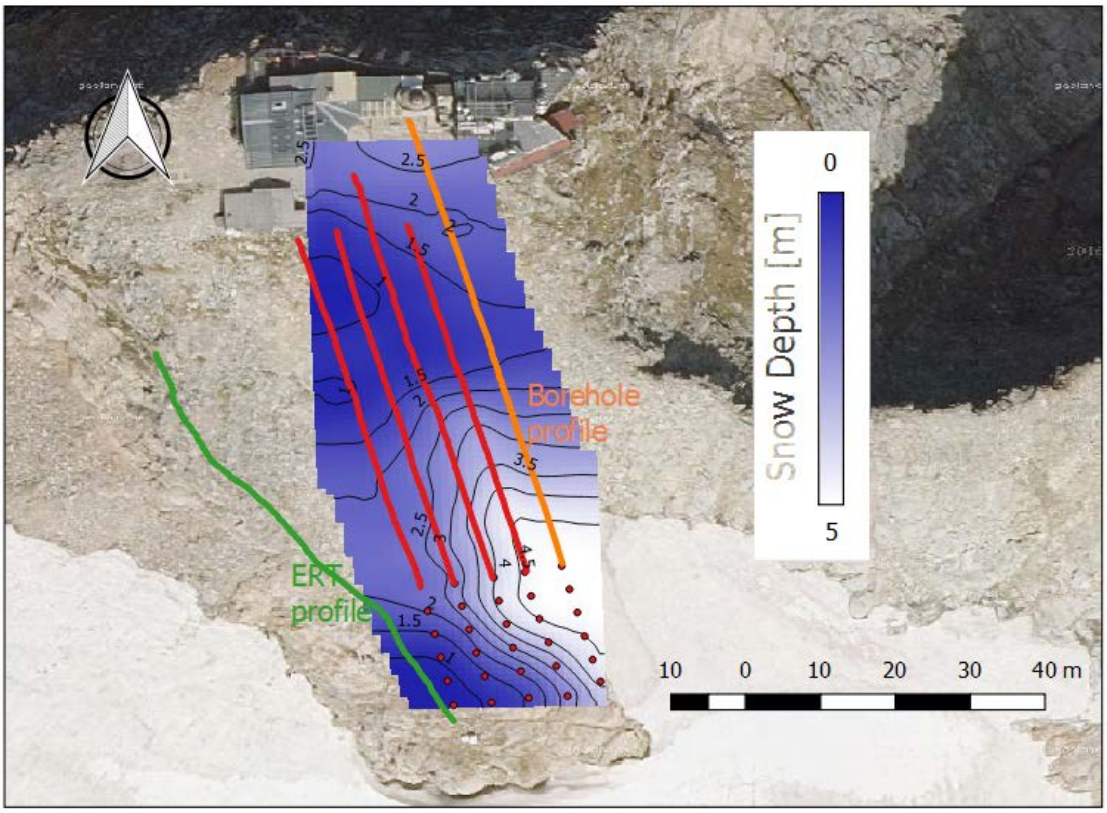

Figure 7-19: Snow depths present at the summit of Sonnblick in May 2017 superimposed on an orthophoto revealing higher snow depths in the lower sector close to the glacier and lower snow depths in the upper summit area, which is in good agreement with experienced snow depths.

As it can be seen in Figure 7-19, the snow depth is highest for the lower summit area close to the glacier Goldbergkees and decreases with increasing slope and altitude. This approximation is in good agreement with the experienced snow depths during our field survey.

The final result is presented in Figure 7-20, which shows the depth to the permafrost body interpolated over the whole raster area. From this outcome, we can state that in the middle part of the survey area the permafrost table is situated in a depth between 4 and 5 metres. As mentioned previously, in the upper area the low depth values could be related to building constructions of the Sonnblick observatory and are not reliable due to low SNRs. In the lower area, the glacier ice is interpreted as permafrost for simplifying reasons, therefore only the middle

part of the grid gives consistent and adequate approximations for a possible depth of the permafrost table. Additionally, a deeper permafrost table is obtained in the eastern part of the survey area compared to the western part, which is indicated by the colour coding and the contour lines in Figure 7-20.

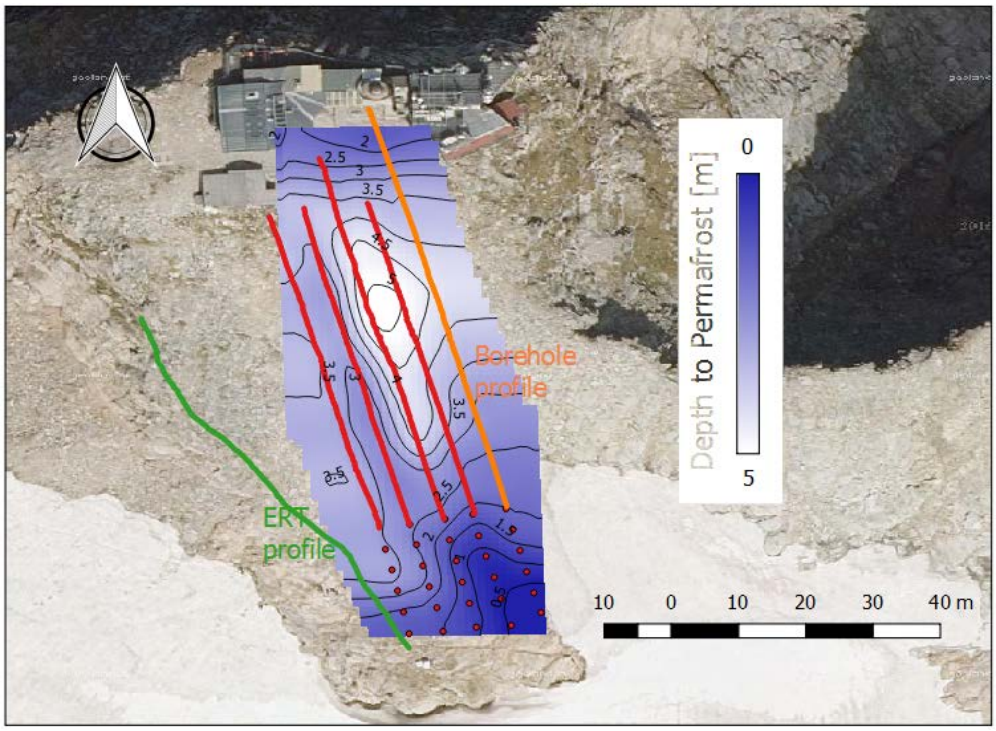

Figure 7-20: Depth to permafrost interpolated for the area spanned by the 5 borehole profiles

7.6 Comparison of different times

Two datasets acquired with 400 MHz antenna at different times are presented in Figure 7-21.

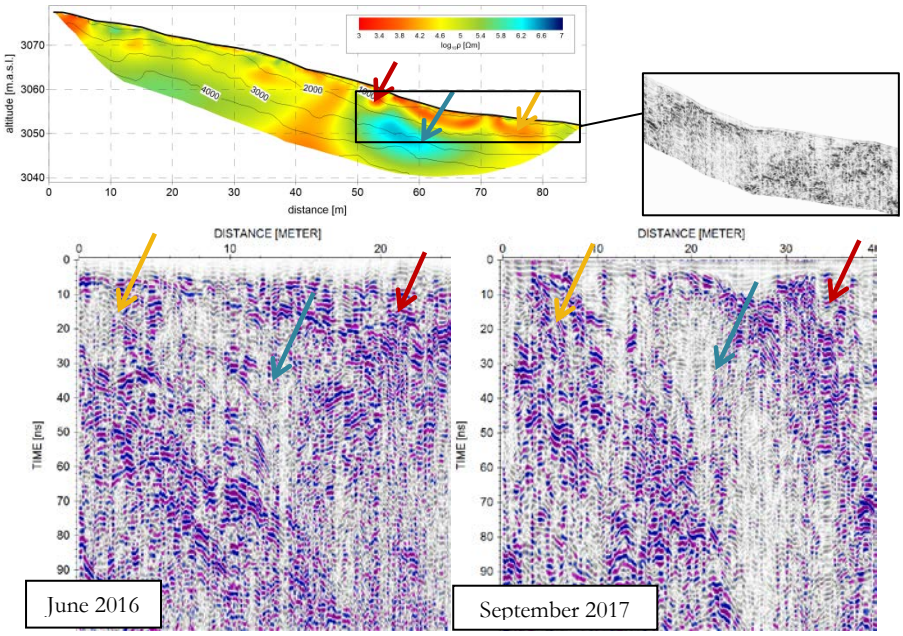

Figure 7-21: GPR data acquired along the ERT profile with 400 MHz antenna at different times of the year

The data were collected along the ERT profile with a maximum accessible profile length of 40m due to the dangerous slope in winter. Both datasets show a high reflection coefficient for low resistivity zones of ~4Ωm (red and orange arrow) and a lower reflection coefficient for higher resistivity values of ~6Ωm (blue arrow). The low resistivity zone in the near subsurface is associated with loose boulders containing water voids, thus exhibiting multiple reflections within the voids. The high resistivity zone is related to permafrost with no reflections and no losses observed in autumn. When comparing the two dates, the reflections within the estimated permafrost part are higher in June, which could be due to the thawing of the active layer.

7.7 Validation with Temperature data

Time series of permafrost temperatures of the three boreholes at several depths are available for the period 2008 to 2016. An exemplary contour plot of the measured temperature data of the borehole close to the glacier for the year 2016 is demonstrated in Figure 7-22. Such temperature plots indicate that in winter, the ground is frozen to the surface, whereas during summer the active layer thaws and the permafrost table is defined by negative ground temperatures. For the comparison of temperature data with 3D GPR modelling results, the -1°C contour line is a good representation of the depth to the permafrost table.

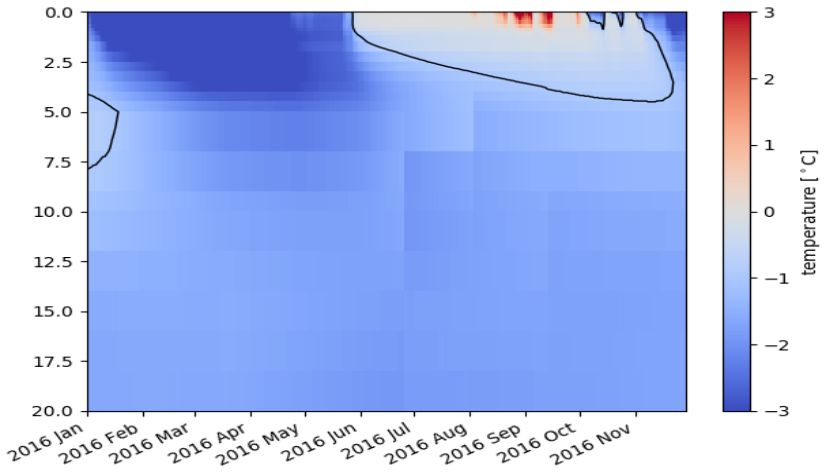

Figure 7-22: Exemplary time series of borehole temperatures at depths up to 20m measured in the borehole close to the glacier at Hoher Sonnblick for the period Jannuary 2016 to Dezember 2016.

Therefore, the deepest point on the -1°C - contour line is picked for each year and each borehole and the mean and median are calculated and demonstrated in table 7-2.

Table 7-2: Overview of depth values for -1°C contour line from three boreholes in alpine permafrost and calculated median and RMS values over the years and over the three boreholes showing a median of 5m and a RMS of 5.43m

Year	Borehole 1 [m]	Borehole 2 [m]	Borehole 3 [m]	Median [m]	Mean [m]
2008	5.5	4.75	5	5	5.08
2009	5	-	-	5	5
2010	5	5	5.25	5	5.08
2011	5	5	4.5	5	4.83
2012	-	-	5	5	5
2013	6.25	-	5	5.63	5.63
2014	7	5	5.25	5.25	5.75
2015	6.75	-	7.5	7.13	7.13
2016	6.25	5	4.75	5	5.33
Median [m]	**5.88**	**5**	**5**	**5**	**5.43**
Mean [m]	**~5.97**	**4.95**	**~5.28**		

The results of Table 7-2 indicate a median of 5m for the second and the third borehole which is in good alignment with the permafrost table defined by GPR.

8 Conclusions and Outlook

In this study, synthetic models have been presented and compared to measured GPR data collected in different media and for different applications. The results demonstrate that GPR modelling provides information not accessible with solely interpretation of processed data for the characterisation of permafrost sites.

Although promising for the quantification of contaminants in porous media, the modelling of GPR data in heterogeneous debris-covered alpine environments is challenging. As expected due to the complexity of alpine permafrost soils, the models need to take into account the large number of discontinuities observed in the GPR data, related to fractures and lithological contacts. Boulders within the debris layer can act as a significant source of noise, as they create hyperbolic diffraction patterns masking reflections of interest.

Despite these limitations, modelling results at the summit of Hoher Sonnblick demonstrate the applicability of the modelling approach to consider signal reflection and attenuation to validate the interpreted lithologic and thermal units within permafrost environments. The tests performed on several synthetic and field data sets (at different frequencies) allow a detailed analysis in order to obtain reliable results of the depth to the permafrost body. Modelling results have been compared to borehole temperature data which reveal consistency.

It would be interesting to install another ERT profile in close proximity to the borehole profiles, where the accessibility with GPR is better in winter conditions. This would ensure a direct comparison between GPR and ERT for similar locations, resulting in electrical conductivity values representative for the GPR model under investigation. Furthermore, it is recommended to test this modelling approach in different permafrost environments and for different times of the year.

Structural information obtained from the 2D-models is used in further investigations to refine the initial model for the tomographic inversion of Refraction Seismic Tomography data (RST). The synthetic RST imaging results should allow for a better understanding of the influence of GPR constraints and the limitations of this joint approach.

9 Abbildungsverzeichnis

9.1 Bibliography

Alteköster, Carsten Albert. 2004. 'Untersuchungen zur Reproduzierbarkeit von Bodenradarmessungen', Universitäts-und Landesbibliothek Bonn.

Artemov, VG, and AA Volkov. 2014. 'Water and ice dielectric spectra scaling at 0 C', *Ferroelectrics*, 466: 158-65.

Atekwana, Estella A, and Eliot A Atekwana. 2010. 'Geophysical signatures of microbial activity at hydrocarbon contaminated sites: A review', *Surveys in Geophysics*, 31: 247-83.

Berthling, I, B Etzelmuller, H Farbrot, K Isaksen, M Wale, and R Odegard. 2008. "GPR soundings of rock glaciers on Svalbard." In.: Cambridge University Press.

Butler, Dwain K. 2005. *Near-surface geophysics* (Society of Exploration Geophysicists).

Cassidy, Nigel J. 2009. *Electrical and magnetic properties of rocks, soils and fluids* (chapter).

Dobinski, Wojciech. 2011. 'Permafrost', *Earth-Science Reviews*, 108: 158-69.

Everett, Mark E. 2013. *Near-surface applied geophysics* (Cambridge University Press).

Flores-Orozco, Adrián, Andreas Kemna, Christoph Oberdörster, Ludwig Zschornack, Carsten Leven, Peter Dietrich, and Holger Weiss. 2012. 'Delineation of subsurface hydrocarbon contamination at a former hydrogenation plant using spectral induced polarization imaging', *Journal of Contaminant Hydrology*, 136: 131-44.

Harris, Charles, Lukas U Arenson, Hanne H Christiansen, Bernd Etzelmüller, Regula Frauenfelder, Stephan Gruber, Wilfried Haeberli, Christian Hauck, Martin Hoelzle, and Ole Humlum. 2009. 'Permafrost and climate in Europe: Monitoring and modelling thermal, geomorphological and geotechnical responses', *Earth-Science Reviews*, 92: 117-71.

Hauck, Christian. 2001. 'Geophysical methods for detecting permafrost in high mountains', Universität München.

Hauck, Christian, and Christof Kneisel. 2008. *Applied geophysics in periglacial environments* (Cambridge University Press Cambridge).

Hausmann, Helmut, Karl Krainer, Ewald Brückl, and Christian Ullrich. 2012. 'Internal structure, ice content and dynamics of Ölgrube and Kaiserberg rock glaciers (Ötztal Alps, Austria) de-termined from geophysical surveys', *Austrian Journal of Earth Sciences*, 105: 12-31.

Hinkel, KM, JA Doolittle, JG Bockheim, FE Nelson, R Paetzold, JM Kimble, and R Travis. 2001. 'Detection of subsurface permafrost features with ground-penetrating radar, Barrow, Alaska', *Permafrost and Periglacial Processes*, 12: 179-90.

Kneisel, Christof, Christian Hauck, Richard Fortier, and Brian Moorman. 2008. 'Advances in geophysical methods for permafrost investigations', *Permafrost and Periglacial Processes*, 19: 157-78.

Knödel, Klaus, Heinrich Krummel, and Gerhard Lange. 2013. *Handbuch zur Erkundung des Untergrundes von Deponien und Altlasten: Band 3: Geophysik* (Springer-Verlag).

Krainer, Karl. 2007. 'Permafrost und Naturgefahren in Österreich', *Online-Fachzeitschrift des Bundesministeriums für Land-und Forstwirtschaft*.

Krautblatter, Michael, Sarah Verleysdonk, Adrián Flores-Orozco, and Andreas Kemna. 2010. 'Temperature-calibrated imaging of seasonal changes in permafrost rock walls by quantitative electrical resistivity tomography (Zugspitze, German/Austrian Alps)', *Journal of Geophysical Research: Earth Surface*, 115.

Massinger, Gerhard, and Franz Michlmayr. *Die Uferstrukturen der Donauinsel im Stauraum Freudenau* (na).

Moorman, Brian, Stephen Robinson, and Margo Burgess. 2007. 'Imaging near-surface permafrost structure and characteristics with Ground-Penetrating Radar', *CSEG Recorder J*, 32: 23-30.

Mühll, Daniel Vonder, Christian Hauck, Hansueli Gubler, Robert McDonald, and Nick Russill. 2001. 'New geophysical methods of investigating the nature and distribution of mountain permafrost with special reference to radiometry techniques', *Permafrost and Periglacial Processes*, 12: 27-38.

Persico, Raffaele. 2014. *Introduction to ground penetrating radar: inverse scattering and data processing* (John Wiley & Sons).

Reynolds, John M. 2011. *An introduction to applied and environmental geophysics* (John Wiley & Sons).

Rogger, M, GB Chirico, H Hausmann, K Krainer, E Brückl, P Stadler, and G Blöschl. 2017. 'Impact of mountain permafrost on flow path and runoff response in a high alpine catchment', *Water Resources Research*, 53: 1288-308.

Schöner, Wolfgang, Lorenz Boeckli, Helmut Hausmann, Jan-Christoph Otto, Stefan Reisenhofer, Claudia Riedl, and Sirri Seren. 2012. 'Spatial patterns of permafrost at Hoher Sonnblick (Austrian Alps)-extensive field-measurements and modelling approaches'.

Subcommittee, Permafrost. 1988. 'Glossary of permafrost and related ground-ice terms', *Associate Committee on Geotechnical Research, National Research Council of Canada, Ottawa*, 156.

Supper, Robert, David Ottowitz, Birgit Jochum, Alexander Roemer, Stefan Pfeiler, Stefanie Kauer, M Keushnig, and Anna Ita. 2014. 'Geoelectrical monitoring of frozen ground and permafrost in alpine areas: field studies and considerations towards an improved measuring technology', *Near Surface Geophysics*, 12: 93-115.

Ward, Stanley H. 1988. "The resistivity and induced polarization methods." In *Symposium on the Application of Geophysics to Engineering and Environmental Problems 1988*, 109-250. Society of Exploration Geophysicists.